Radboud University Nijmegen

Faculty of Science

Higgs Boson Reconstruction Studies

for the measurement of $pp \to WH \to \ell\nu b\bar{b}$ with the ATLAS Detector at the Large Hadron Collider

Thesis BSc Physics

Author:
Paul Veen

Supervisor:
dr. Frank Filthaut

Second reader:
dr. Harm Schoorlemmer

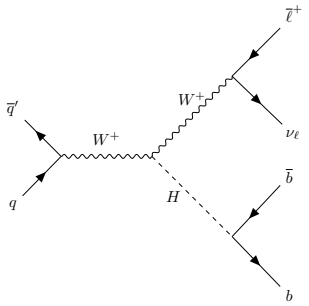

Institute for Mathematics, Astrophysics and Particle Physics
Radboud University

July 2022

Abstract

A comparison of reconstruction techniques for Higgs bosons decaying into a pair of b-quarks is presented using simulated proton-proton collisions at a center-of-mass energy of 13 TeV in the ATLAS detector at the LHC. Simulated $pp \to WH \to \ell\nu b\bar{b}$ events are considered and the Higgs boson is reconstructed either from two jets with a radius parameter of R = 0.4 (resolved), a single jet with a radius parameter of R = 1.0 (boosted) or a single jet with a radius parameter of R = 0.4 (superboosted).

The signal efficiency is calculated as a function of the Higgs boson's transverse momentum for each of the reconstruction algorithms. Even at transverse momenta of the Higgs boson above 800 GeV, the boosted reconstruction technique is 30% more efficient than the superboosted technique. Similar conclusions are drawn when taking into account simulated background processes, where a resolved and boosted combination shows 30% higher sensitivity to the WH signal than a resolved and superboosted combination, not taking into account systematic uncertainties.

Acknowledgments

In the first place, I would like to thank my supervisor, dr. Frank Filthaut, for giving me the possibility to do my Bachelor thesis on such an interesting topic, in the context of the outstanding ATLAS collaboration. I would also like to thank him for finding time to guide me and for reading my thesis. In a similar fashion, I would also like to thank my second reader, dr. Harm Schoorlemmer, for his time and effort.

I want to highlight the amazing guidance I have got from my two daily supervisors, Marion and Brian. It did not matter how often I asked some random question, I would always get a sophisticated answer, and they were always able to find time to help me, even considering their crowded schedules.

Furthermore, I would like to thank my friends for taking their time to listen to me talking about my internship and providing helpful feedback from time to time. Last not least, I would like to thank my parents and my sister for their useful insights and (sometimes near infinite) attention to topics they had never heard of before.

Contents

1 Introduction

Particle physicists are interested in the fundamental nature of the universe at the smallest of scales. For example, what are the building blocks that make up everything that we see, including ourselves? The best answer - at this moment - is given by the *Standard Model (SM) of particle physics*, describing the elementary particles that make up our world and predicting the outcome of experiments to incredible accuracy.

However, it is not complete, as for instance it does not include gravity nor does it predict a Dark Matter candidate.

In order to look for new physics, it is possible to study known processes in the SM very accurately and look at deviations from the theoretical predictions. A candidate for new physics could be the Higgs boson, the last particle of the SM to be experimentally verified, by the ATLAS [1] and CMS [2] collaborations at the Large Hadron Collider (LHC) at CERN, 2012. It is a relatively new particle, connected to all other massive particles in the SM and therefore it is the ideal candidate for studying SM processes and their deviations with experiment.

Such experiments are typically done in particle colliders, like the LHC at CERN. This machine accelerates particles to velocities extremely close to the speed of light in order to collide them at enormous energies. Based on the mass-energy equivalence principle, it is expected that these collisions will create numerous new particles, making it possible to study the sub-atomic structures.

The Higgs boson can be detected by looking at its decay products, as it is very short-lived. About 60% of the time, the Higgs boson will decay to a pair of bottom quarks, which can be observed as two *jets* of particles. This decay channel is called $H \to b\bar{b}$ and will be the main topic of this thesis.

There are different ways to reconstruct these two jets, depending on the energy of the Higgs boson. At low energies, the two jets will be geometrically separated from each other and are typically reconstructed individually (resolved reconstruction). At higher energies, the two jets will become closer, such that at some point they can no longer be reconstructed individually. Instead, the full $H \to b\bar{b}$ decay is reconstructed in a single jet. Depending on the energy, large radius jets (boosted reconstruction) or jets with smaller radius (superboosted reconstruction) can be used. While large radius jets will also work for more collimated $H \to b\bar{b}$ decays, they are more exposed to background contamination due to their large radius. In additions systematic uncertainties for small radius jets are typically smaller than for large radius jets. These points motivate comparing the different reconstruction methods.

The first section after this introduction, section 2, will lay out the theoretical background. In particular, it introduces the Standard Model and the Higgs boson. Section 3 explains the experimental background, regarding the ATLAS detector and jets. At the end of this section, the research question is introduced in more detail. Section 4 discusses the reconstruction methods that will be used to obtain the results. The first part of section 5, studies the efficiency of the different Higgs boson reconstruction techniques, whereas the second part follows with a sensitivity estimate by confronting the simulated signal with background events. Finally the results are discussed in section 6, followed by a conclusion.

2 Theoretical Background

Before the main research question and methods can be introduced, it is first necessary to provide some background on the topic of the Higgs boson and its decay. This is done by introducing the Standard Model of particle physics, which will also explain other concepts relevant to this research.

The Brout-Englert-Higgs mechanism is discussed at the end of this section to provide some background to the topic of the Higgs boson. This discussion is concise and more information can be found in appendix A.

The information presented is roughly based on references [3, 4].

2.1 The Standard Model

The Standard Model is the physical model that describes all elementary particles and their interactions in the current state of our knowledge. It has been tested numerous times and verified to great precision, but it is incapable of uniting gravity and quantum field theory and there are experimental hints, like Dark Matter, that also point at absences in the SM. These are examples of evidence suggesting it is not a 'final' theory.

The Standard Model describes the interactions of fields, the excitation of which can be observed as particles, divided into *fermions* (integer/2 spin) and *bosons* (integer spin). Fermions are "matter particles", they form bound states and eventually all atoms and molecules. Each fermion appears in a doublet of two particles differing by 1 unit charge, e.g. the electron (charge -1) and the electron neutrino (charge 0), or the up-quark (charge +2/3) and down-quark (charge -1/2). These doublets appear three times, the *generations*.

The spin-1 bosons are the "force mediators", they make the electromagnetic (photon), strong (gluon), and weak interactions possible (W^+, W^-, Z). These bosons act on the fermions mentioned before: the photon acts on *electromagnetic charge*, the gluon on *colour charge* (only quarks and gluons have the property *colour*), the W^+ and W^- bosons act on *weak isospin*, and the Z acts on a combination of weak isospin and *weak hypercharge*, emerging from the combined electromagnetic and weak interactions (the electroweak interaction). In addition, the W bosons obey a *chiral symmetry*, which dictates how the particle transforms under a parity transformation. Left-handed particles are affected by the W bosons, while right-handed particles remain indifferent.

Bosons do not only interact with fermions, they can also interact with the other bosons as long as they have the appropriate properties, e.g. the gluons interact with other gluons (colour) and the photon interacts with the W^+ and W^- bosons (electric charge). All particles of the Standard Model and some of their properties can be found in figure 1.

The Higgs boson is unique as it is the only spin-0 (scalar) particle in the Standard Model and it interacts with all massive particles. This particle is a consequence of the scalar doublet Higgs field (i.e. 4 degrees of freedom) introduced in the Standard Model. Through spontaneous symmetry breaking and the Brout-Englert-Higgs mechanism, 3 of the degrees of freedom can be associated with the W and Z masses, and the one remaining with the Higgs boson. The concept of spontaneous symmetry breaking will be explained to some extent in section 2.3
Moreover, it is the last particle of the Standard Model to have been discovered and it will be the main character in this thesis.

2.2 Beyond the Standard Model

The Higgs boson was discovered in 2012 by the ATLAS [1] and CMS [2] collaborations at the Large Hadron Collider (LHC) at CERN, Geneva. It took 40 years to verify the existence of this last part of the SM, because a combination of high energies and sufficient collision rates was required to produce it, which was achieved by the then newly-built LHC. This also implies that there has not been done as much research on the Higgs boson as has been done on the other parts of the Standard Model, while it is connected to all other massive particles in the SM, making the Higgs a very interesting topic of research and potential candidate of *beyond the Standard Model physics*. Noticing that there have not been that many breakthroughs in 'new physics' in the last four decades, it could be rewarding to investigate these Higgs bosons more.
This last point can be expanded upon using figure 2, where the Higgs boson is produced in association with a W boson. In this channel, the W boson is used to eliminate background noise as the leptonic signatures minimise the signal to background ratio (b pair production is very common, but in combination with the leptons it is possible to look specifically for b-quarks originating from $H \to b\bar{b}$ decay).

Clearly, at higher energies the differences between the Standard Model predictions and another[1] SM extension diverge, so it makes sense to look at high Higgs *transverse momentum* p_T^H[2] - which gives an idea of the energies involved in the interaction - in order to probe new physics.

The growing behaviour of this extension is actually typical for the SMEFT (Standard Model Effective Field Theory) approach shown in figure 2, based on the hypothetical existence of much heavier particles that cannot be produced currently, but the interactions may be sensitive to the onset of their effects.

[1] It is important to emphasise that this is just some possible extension to the Standard Model.

[2] The transverse momentum is defined as the component of the momentum transverse to the beam axis. Transverse momentum is more properly introduced in the experimental background section (section 3.2.1).

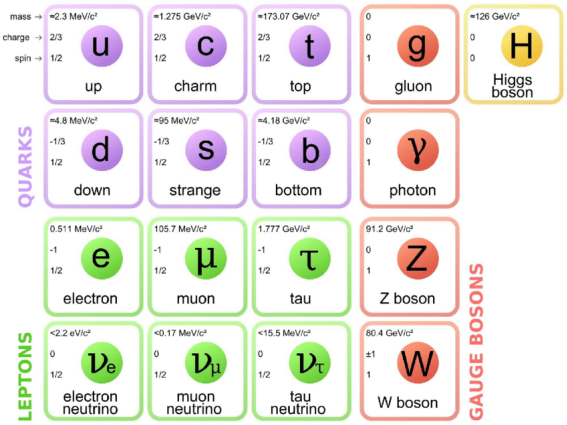

Figure 1: The particles of the Standard Model. The properties mass, charge, and spin are displayed [5].

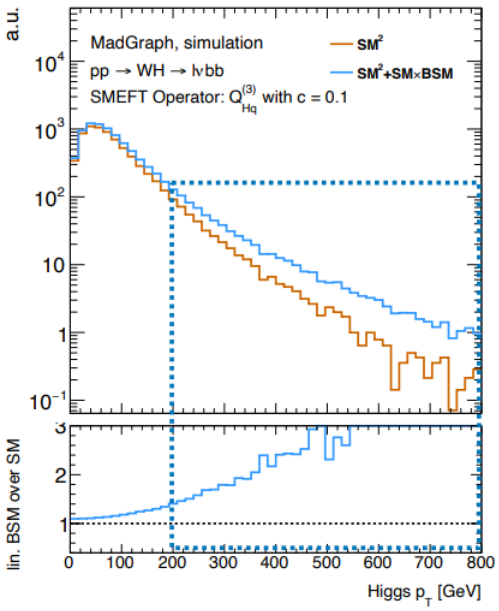

Figure 2: In this plot the differential cross section as a function of the Higgs boson transverse momentum p_T and the difference in Standard Model prediction and another Standard Model extension is shown. Specifically, using the SMEFT approach (Standard Model Effective Field Theory) [6].

The main decay mode of the Higgs boson is the Higgs to bottom quark, anti-bottom quark process, $H \to b\bar{b}$, with a branching ratio of $(58.2 \pm 1.2)\%$, as predicted by the SM. [7]. Although this could differ if SMEFT is considered.

There are various interactions to get to this decay, this thesis focuses on the $pp \to W\ H \to \ell\nu b\bar{b}$ 1-lepton channel, as shown below using a *Feynman diagram*, figure 3.
Note that there exist other similar decay channels, like $pp \to Z\ H \to \bar{\nu}\nu b\bar{b}$ 0-lepton and $pp \to Z\ H \to \bar{\ell}\ell b\bar{b}$ 2-lepton, that could also be used to study $H \to b\bar{b}$. These have been displayed in figure 4.

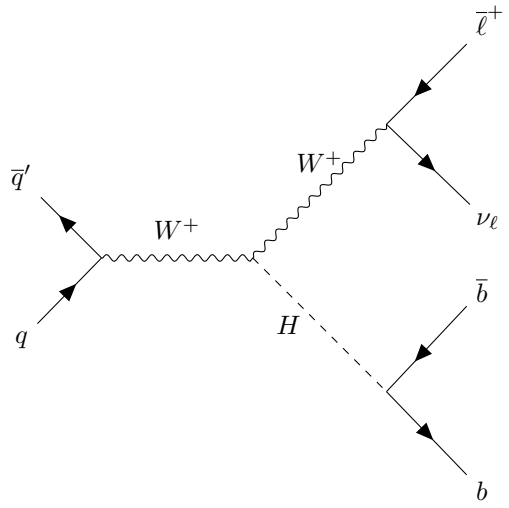

Figure 3: Example first-order Feynman diagram of $pp \to W\ H \to \bar{\ell}\nu b\bar{b}$ decay. The q' indicates a quark differing 1 unit charge from the other quark q. There exists also a conjugate variant with W^- bosons, giving rise to a lepton and an anti-neutrino pair.

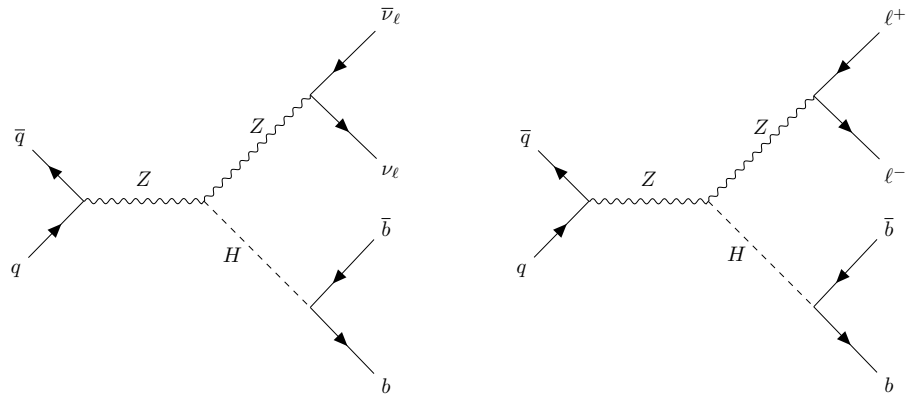

a) $pp \to Z\ H \to \bar{\nu}\nu b\bar{b}$ 0-lepton channel b) $pp \to Z\ H \to \bar{\ell}\ell b\bar{b}$ 2-lepton channel

Figure 4: Example first-order Feynman diagrams of the Higgs boson that have the same structure as the decay considered in this thesis (figure 3).

Two important observations can be made regarding the b-quark pair that originates from the Higgs boson in the $H \to b\bar{b}$ decay:

- The b-quarks are 3th generation particles and therefore have high mass (rest-energy) relative to the other quarks and will decay via the weak interaction to their energetically stabler variants of the 2nd generation (strange and charm) all the way to the 1st generation (up and down).
- Quantum Chromodynamics (QCD) dictates that quarks must always be confined; they must always form colourless bound states, *hadrons*. In the case of the b-quarks, these are called b-hadrons.

From the first fact, it is derived that b-quarks are unstable and decay. From the second, it follows that quarks do not propagate freely and are observed as *jets* of colourless particles, which can happen as the energy stored in the gluon field is sufficient to produce new $q\bar{q}$ pairs. This process is called *hadronisation*.

Jets are used to understand the properties of interactions involving quarks in the final state and in this thesis they prove to be crucial to study the $H \to b\bar{b}$ decay. Jets will be discussed in more detail in section 3.3.

This discussion leads to concepts called $H \to b\bar{b}$ *reconstruction strategies*. From the Feynman diagram introduced in section 2.2, it is seen that the Higgs decays into a b-quark pair. It is known from relativistic kinematics that at low energies of the Higgs boson these jets originating from the quarks start out rather well-separated, but at higher energies they get closer and will eventually overlap. The events with overlapping jets need a different reconstruction than the events where the jets are further apart, therefore, two different reconstruction strategies have to be introduced. These are called the *resolved reconstruction* and *boosted reconstruction* respectively. The techniques have successfully been used in the past, see reference [8] for the *resolved* reconstruction and reference [9] for the *boosted* reconstruction. Both reconstructions are illustrated in figure 5.

The claims regarding the jet behaviour as a function of the energy will be supported by results from simulations in the results section (section 5.1.2).

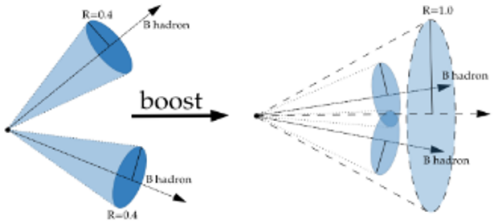

Figure 5: Jet reconstructions. Left: resolved reconstruction, characterised by two small-R = 0.4 cones. Right: boosted reconstruction, characterised by one large-R = 1.0 cone, where R is the radius parameter of the cone. This radius parameter can be interpreted as the size of the cone, but it is explained in more detail in section 3.3. The image can be found in reference [6].

2.3 The Brout-Englert-Higgs Mechanism

This section will give a brief overview regarding the core idea of the Brout-Englert-Higgs mechanism, the phenomenon of *symmetry breaking*. It is independent from the main text, but it provides background for the Higgs boson studied in this thesis.

A more complete review can be found in appendix A.

Suppose ϕ is a real scalar (spin-0) field[3] with potential

$$V(\phi) = \frac{1}{2}\mu^2\phi^2 + \frac{1}{4}\lambda\phi^4 \tag{2.1}$$

Then the *Lagrangian* of this theory becomes[4]

$$\mathcal{L} = \frac{1}{2}(\partial_\mu\phi)(\partial^\mu\phi) - V(\phi) \tag{2.2}$$

Where $\frac{1}{2}(\partial_\mu\phi)(\partial^\mu\phi)$ is the kinetic term, μ^2 can be interpreted as a square of a mass, and λ is related to the (self-) interaction strength.

As can be seen in plot 6, the shape of the potential depends on the sign of μ^2.

In the case $\mu^2 > 0$, the potential has a minimum at $\phi = 0$ and it follows that the Lagrangian describes a spin-0 particle with mass μ.

The interesting case is when $\mu^2 < 0$, because then there is a minimum, called the *vacuum expectation value* obtained from setting $\frac{dV(\phi)}{d\phi} = 0$:

$$\phi \equiv \pm v = \pm\sqrt{\frac{-\mu^2}{\lambda}} \tag{2.3}$$

Without loss of generality, ϕ can be expanded around v i.e. $\phi = v + \eta$ for some perturbation η. Then the Lagrangian (6.2) becomes, using (6.3):

$$\begin{aligned}
\mathcal{L}(\eta) &= \frac{1}{2}(\partial_\mu\eta)(\partial^\mu\eta) - V(\eta) \\
&= \frac{1}{2}(\partial_\mu\eta)(\partial^\mu\eta) - \frac{1}{2}\mu^2(v+\eta)^2 - \frac{1}{4}\lambda(v+\eta)^4 \\
&= \frac{1}{2}(\partial_\mu\eta)(\partial^\mu\eta) - \lambda v^2\eta^2 - \lambda v\eta^3 - \frac{1}{4}\lambda\eta^4 + \frac{1}{4}\lambda v^4
\end{aligned} \tag{2.4}$$

where the last term is a constant and might as well be ignored in the Lagrangian, as the Euler-Lagrange equations are not affected by constants.

This new Lagrangian can be compared one-to-one with (6.2), if it is written in the following form:

$$\mathcal{L}(\eta) = \frac{1}{2}(\partial_\mu\eta)(\partial^\mu\eta) - \frac{1}{2}m_\eta^2\eta^2 - V(\eta) \tag{2.5}$$

with $m_\eta^2 = 2\lambda v^2 = -2\mu^2$ a mass term, and $V(\eta) = \lambda v\eta^3 + \frac{1}{4}\lambda\eta^4$ a potential term.

The original Lagrangian had a potential term with a vacuum expectation value minimum which could be expanded around, breaking the symmetry of the Lagrangian. By some clever manipulations and reinterpreting the symmetry-broken Lagrangian, this introduces a new mass term m_η and a potential $V(\eta)$ term, including a new tri-linear Higgs interaction. Although a relatively simple calculation, it lies at the foundation of the full Higgs Mechanism, and the idea remains the same throughout the full derivation.

[3] This is a simplified example. In the SM, the field is a complex doublet, which is discussed in appendix A

[4] Summation over $\mu = 0, 1, 2, 3$ implied, with metric $g_{\mu\nu} = diag(1, -1, -1, -1)$

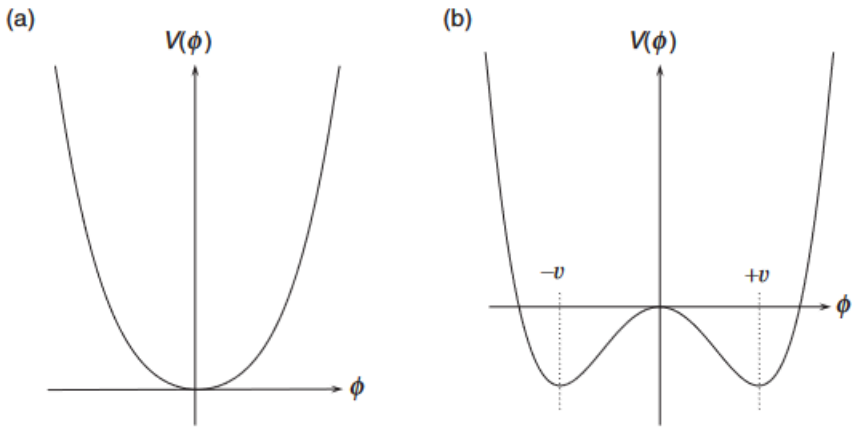

Figure 6: The potential $V(\phi) = \frac{1}{2}\mu^2\phi^2 + \frac{1}{4}\lambda\phi^4$ plotted for $\mu^2 > 0$ (a) and $\mu^2 < 0$ (b) [4].

3 Experimental Background

The focus is shifted to the experimental background, as that will cover the foundations of the research done in this thesis. The ATLAS detector as well as the experimental analysis aspects of jets will be highlighted.

The following section, *Higgs boson reconstruction studies* (section 4), will then describe how to obtain results using the methods discussed in this section.

3.1 The Large Hadron Collider

The Large Hadron Collider (LHC) [10] is the largest and most powerful particle collider in the world, extending the frontiers of particle physics with its unprecedented high energy and luminosity. It consists of a 27 km ring where particles are accelerated to collide at an energy of 13 TeV, 4 billion times per second. The collider started operating in 2008 and has since made numerous discoveries, the most relevant for this thesis being the experimental discovery of the Higgs boson by the ATLAS (A Toroidal LHC ApparatuS) [11] and CMS (Compact Muon Solenoid) [12] experiments in 2012.

Other experiments are no less important, being ALICE (A Large Ion Collider Experiment) [13] focussing on heavy-ion physics to study a phenomenon called quark-gluon plasmas, and LHCb (Large Hadron Collider beauty) [14] studying hadrons containing heavy-flavour quarks (charm, bottom, and top quarks).

The ATLAS experiment has been particularly interested in measuring predicted decay modes for the Higgs particle, its properties, and more open questions, like whether there is only one Higgs or whether there might be more. This thesis studies simulations of Higgs bosons produced in pp collisions at the LHC that are recorded by the ATLAS experiment.

3.2 The ATLAS Experiment

ATLAS is a multi-purpose experiment designed to measure a wide range of physics. The detector sits in a cavern at 100 meters below surface level, and with dimensions 46 m $\times$ 25 m $\times$ 25 m and 7000 tonnes weight, it is the largest detector on Earth. It is not limited to measuring only the Higgs particle, it also investigates Dark Matter, extra dimensions, and the experiment gets more precise measurements of constants used in the Standard Model.

3.2.1 The ATLAS Detector

ATLAS is designed to detect particles using different sub-detectors with different technologies. The design of the detector has been guided in particular by the search of the Higgs boson and this can be seen for the detector is optimised to find the decay products of the dominant Higgs decay channels.

The inner detector consists of a high-resolution semiconductor pixel and strip detectors in its inner part and straw-tube[5] detectors in its outer part. These detectors allow for pattern recognition, momentum and vertex[6] measurements, and the identification of electrons. The electromagnetic energy measurements are done using several types of high granularity Liquid-argon (LAr) calorimeters[7].

[5] Straw-detectors use a long tube filled with a gas and a wire through the center such that an electric potential is maintained with the walls of the tube. When particles go through the detector, the gas becomes ionised and this produces a current.

[6] A vertex is defined as the point at which an interaction occurred.

[7] A calorimeter is a device that can measure heat, and therefore energy, of particles.

Muons are charged particles and will leave ionisation signals in the inner detector and calorimeters. These can be used to reconstruct their trajectories, but do not typically unambiguously identify the muons. Therefore, another detector is required, the muon spectrometer, which surrounds the other spectrometers. The construction of the muon spectrometer as an air-core toroid system and two end-cap magnets allows for strong bending in a large volume.

Multiple-scattering effects are minimised by air that is present in the volume and the muons can, therefore, be detected with high precision.
The various parts of the ATLAS detector have been displayed in the computer generated cross-section figure 7.

The ATLAS detector uses a right-handed coordinate system which is convenient for studying the collisions in the LHC. The origin of these coordinates is defined as the nominal interaction point, where particles collide. The z-axis is defined by the beam direction, the x-axis is defined as pointing towards the center of the LHC ring and the y-axis is defined as pointing upwards. Naturally, these axes are orthogonal.

The azimuthal angle ϕ is defined as the angle around the beam axis, while the polar angle θ is the angle from the beam axis. The *pseudorapidity* is defined as $\eta = -\ln tan(\theta/2)$ and for massless objects it is equal to the rapidity $y = \frac{1}{2}\frac{E+p_z}{E-p_z}$, where E is the energy of the particle and p_z the component of its momentum along the beam axis (using natural units where $\hbar = c = 1$). They are also approximately equal for massive particles with $\frac{E}{m} >> 1$, with m being the *rest mass*. A proof can be found in reference [4].

In this thesis, the *transverse momentum* p_T is used and it is defined as the component of the momentum transverse to the beam direction. Another quantity that will be used is the radial distance *delta-R* defined as $\Delta R = \sqrt{\Delta\eta^2 + \Delta\phi^2}$ where $\Delta\eta = (\eta_1 - \eta_2)$ for two objects 1 and 2. $\Delta\phi$ is defined similarly.

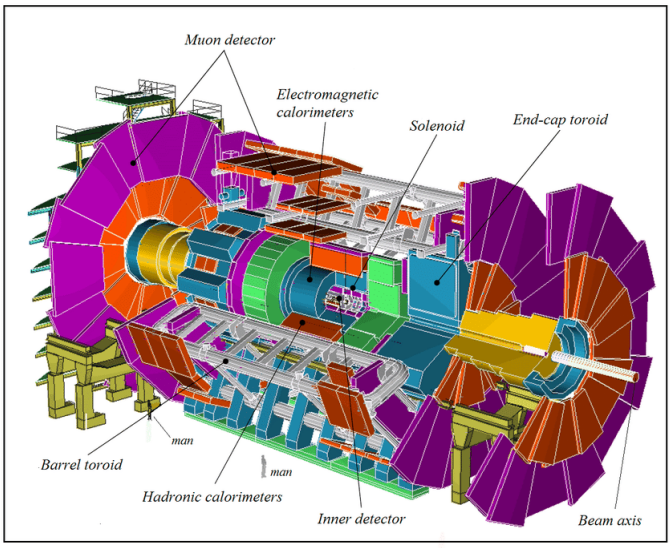

Figure 7: Computer generated cross-section of the ATLAS detector. Several parts are indicated in the figure [15].

3.3 Jets

This section is based on references [6, 7, 9, 16, 17]

Jets have already been introduced in the theoretical background (section 2), but it is necessary to include a more sophisticated treatment of jets from an experimental point of view, in order to understand the reconstruction process of the $H \to b\bar{b}$ decay, using the ATLAS detector.

The jets are reconstructed from energy deposits in the calorimeters as well as charged-particle momenta, taking the most precise information, to be reconstructed using the *anti-k_t* jet algorithm [16]. This algorithm uses the distances d_{ij} between two objects i and j, as well as the distance d_{iB} between an object i and the beam B. The algorithm then finds the smallest of the distances. If this happens to be d_{iB}, it defines i as a jet. Otherwise, the object is called a pseudojet and the objects i and j are recombined, the distances are recalculated and the process starts again. This iteration is terminated when there are no objects left.
The distances are defined as follows:

$$d_{ij} = min\left\{\frac{1}{k_{ti}^2}, \frac{1}{k_{tj}^2}\right\}\frac{\Delta_{ij}^2}{R^2} \tag{3.1a}$$

$$d_{iB} = \frac{1}{k_{ti}^2} \tag{3.1b}$$

with $\Delta_{ij}^2 = (y_i^2 - y_j^2) + (\phi_i^2 - \phi_j^2)$ and transverse momentum k_t[8], rapidity y, azimuthal angle ϕ and radial distance R as before.

From this *anti-k_t* algorithm, the following jet collections are used in the reconstruction:

- Small-R jets, defined by $R = 0.4$
- Large-R jets, defined by $R = 1.0$
- Variable-R (VR) jets, defined by a momentum dependent $R \sim 1/p_T$

The small-R and large-R jets will be used in the reconstruction methods section (section 4). VR jets will be needed for flavour tagging in the analysis on reconstructed level (section 4.4) and are explained briefly below (section 3.3.1).

3.3.1 Track Jets

Track jets are used in a process called *b-tagging* to identify b-jet events. The track jets used in the reconstruction of the Higgs boson in this decay are the VR track jets mentioned above. These jets are constructed by setting $R = R(p_T)$ transverse momentum dependent in the *anti-k_t* algorithm and including cut-offs R_{min} and R_{max}. Explicitly,

$$\begin{aligned} R(p_T) &= 30\ GeV/p_T \\ R \in [R_{min}, R_{max}] &= [0.02, 0.4] \end{aligned} \tag{3.2}$$

which is the optimised choice of parameters for the decay mode considered in this thesis.

[8] In this thesis, the notation p_T is prefered for the transverse momentum, but the notation k_t is illuminating in this case, as it clarifies the algorithm name *anti-k_t*.

3.4 Reconstruction Methods

Now that the concept of jets has been introduced, it is possible to discuss Higgs boson reconstruction techniques, where jets are used to reconstruct the $H \to b\bar{b}$ decay. The resolved and boosted reconstruction techniques are described in a technical way and their discussion will be followed by the introduction of a new reconstruction method, the *superboosted* reconstruction. This method is discussed as well and from there the main research question of this thesis can be formulated.

The main idea of the Higgs boson reconstruction depends on the fact that jets are formed in mostly one direction. In a sense, a cone can be drawn over the jets, covering most of them. This cone is constructed using the geometrical distance delta-R between a jet and the jet-axis, where delta-R is defined as before, $\Delta R = \sqrt{\Delta\eta^2 + \Delta\phi^2}$.

As the jets start overlapping when the energy increases, it is necessary to use different methods at different energies.

Using the distance between a jet and the jet-axis, it is now possible to quantitatively define the resolved and boosted reconstructions.

The resolved reconstruction is characterised by two distinct small-R jets and plays a role from $p_T^V = 150$ GeV to $p_T^V = 250$ GeV.

This is the reconstruction where delta-R > 0.4 (between a jet and the jet-axis).

The boosted reconstruction is defined by the energies where the jets start to overlap to where they are essentially fully overlapped, typically from $p_T^V > 250$ GeV. One large-R jet is reconstructed instead of the two overlapping small-R jets.

In this case, Delta-R > 1.0 (between a jet and the jet-axis).

There are additional restrictions that define these regimes, motivated by physical considerations, which will be explained when the full Higgs boson reconstruction algorithm is discussed (section 4.3). Moreover, the claims on the energies will be justified to some extent in the results section (section 5).

As mentioned before, this analysis has its flaws.

The main issues with the current delta-R method:

1. At higher energies (from around 800 GeV), the jets start overlapping more drastically and delta-R between two b-objects will become smaller, while still being reconstructed with large-R jets. This means that the boosted reconstruction works well at medium and high energies, but at very high energies it is possible to consider using smaller jets, because larger jets are exposed to more background contamination.

2. Small-R jets perform best at low energies, so they can always be used. However, at high energies, the resolved analysis becomes inefficient and another method is required. Boosted is a good choice, but has the downside of introducing a second type of jets with corresponding uncertainties, so it would be prefered to have only one type of jets.

3. It remains unclear what happens in the overlap region. The process turns from two jets to one jet and it is impossible to define exactly where the jets overlap, when the reconstruction should switch from resolved to boosted, and whether this transition is smooth or not.

The proposed alternative is to introduce another reconstruction to compare with these former reconstructions, which is the *superboosted reconstruction*.

This superboosted reconstruction is an extrapolation of the boosted reconstruction technique to very high energies. Only one small-R jet is used, containing two b-quarks, as the small-R jets should cover the overlapped jets at very high energies. An important difference with the resolved reconstruction - that also uses small-R jets - is that these jets are not *distinct* in the superboosted reconstruction. They should contain both b-quarks in one jet, while the resolved reconstruction uses two jets that cover one b-quark each per event.

However, there are still potential issues with this superboosted reconstruction:

1. Events that are reconstructed by the superboosted method are always reconstructed by boosted as well, as the small-R jets are contained in the large-R jets. Necessarily, the efficiency (the number of events that the reconstruction can find) of superboosted will be lower than the efficiency of the boosted reconstruction.

2. For the sensitivity of the reconstruction it is also important how the method works on the backgrounds (events that look like $H \to b\bar{b}$). So even if the efficiencies are the same, superboosted could have a better sensitivity if it is able to discriminate the signal (the actual $H \to b\bar{b}$ events) more from the backgrounds.

It is now possible to formulate the goal of this thesis in a more technical manner: the goal of this thesis is to study the *efficiency* and the *sensitivity* of the superboosted reconstruction compared to the boosted reconstruction at high p_T^H.

Both reconstructions methods are sketched in figure 8.

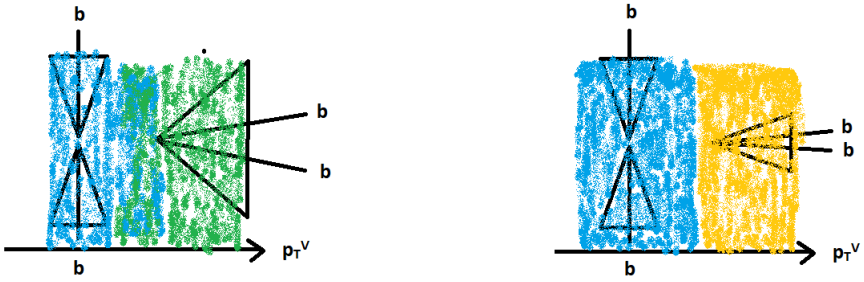

Figure 8: The three reconstruction strategies are used in two ways, both of which are drawn above. Left: resolved (blue) and boosted (green). The resolved reconstruction uses two small-R cones to fit the jets at low energy and the boosted reconstruction uses one large-R cone to fit the jets at high energy. There is a clear overlap between the two reconstructions (indicated by blue/green). Right: resolved (blue) and superboosted (yellow). The resolved reconstruction is the same as before, but the superboosted reconstruction is different from boosted as it uses a small-R cone instead of a large-R cone to fit the two jets at high energy. A clear advantage is that this only requires small-R jets, which are better optimised than large-R jets.

4 Higgs boson reconstruction studies

In this section the different reconstructions will be discussed and their characterisations will be made clear. The focus is more on the general idea than it is on rigorous code explaining: physical considerations will be explained and how they are reflected in the code used.

Two different types of simulations have been used in this analysis; the truth simulation and the reconstructed (reco) simulation. Analysis on truth level is done using Monte Carlo simulations such that all parameters in an interaction are known. Analysis on reco level in addition also simulates the full detector and looks as if it were real data, in the sense that it can be compared to experimental data, while the truth level does not take the detector into account.

Truth simulations are usually called *generator-level simulations* in the literature.

4.1 pyROOT and SWAN

All simulations and reconstruction studies were done using the pyROOT [18] Python interface, which directly grants access to all of ROOT C++ [19], which is an extensive particle physics oriented C++ library that makes the data analysis on the simulations possible, and has built-in functions necessary for the analysis. In order to compile pyROOT and to import the truth and reco data files, the CERN Jupyter interface SWAN [20] was used. On top of the fact that SWAN grants easy access to all of the ROOT libraries, it also supports cloud storage and smooth sharing of data.

4.2 General Analysis

The general idea behind the algorithm is straightforward. First, Boolean returning functions are defined that check for all conditions on a certain reconstruction. These functions are named *resolved_regime*, *boosted_regime*, and *superboosted_regime* and correspond to the regimes discussed earlier (section 3.4). From these functions, different Boolean (AND, OR, NOT, etc.) combinations can be made that result in various types of plots.

Subsequently, after defining the functions, histograms are initialised for the necessary variables that will be plotted. These histograms are filled based on whether events from the simulation pass certain logical combinations of the reconstructions, e.g. if

$$\textit{resolved\_regime}() \text{ and } \textit{boosted\_regime}() \text{ and not } \textit{superboosted\_regime}()$$

are passed, then the histogram belonging to resolved and boosted (and not superboosted) is filled, as well as a histogram that will contain all events that are passed in some reconstruction, in order to create *fraction/total passed events* plots, which will be useful to compare the reconstructions relative to each other.

This mechanism has been drawn in figure 9.

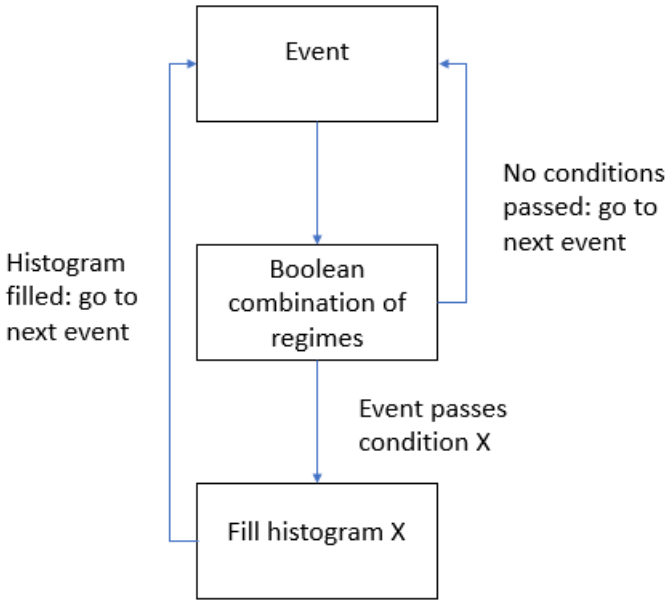

Figure 9: Flow Chart visualising the general idea of the jet analysis algorithm

4.3 Analysis on truth level

The resolved, boosted, and superboosted reconstructions have already been introduced in the previous section, but they can be improved if physical motivations are taken into account.

Considerations regarding the number of jets, the transverse momentum of the jets and vector boson are as follows:

- 2 or 3 small jets for the resolved reconstruction with jet $p_T > 20$ GeV, as below this threshold, they are not calibrated. The reconstruction requires 2 jets, but 3 can be used as inputs. Multiple jets as inputs can also be done in the boosted and superboosted analysis methods. However, only higher order QCD effects can add more than 2 jets. At 4 or more jets, the higher order background effects become too large to add any sensitivity.

- 1 large jet in the boosted reconstruction with jet $p_T > 250$ GeV because the two b-quarks at lower energy are too far apart to be reconstructed with large-R jets.

- 1 small jet, containing 2 b-hadrons, in the superboosted reconstruction with jet $p_T > 20$ GeV as this allows comparison with both the resolved and the superboosted reconstruction. It is important to highlight the difference with the resolved reconstruction in the sense that the new reconstruction jets should contain 2 b-hadrons each, while this does not need to be true in the resolved case, where just one b-hadron per small jet is required.

- More generally, conditions on the lower bounds of the energies prevent background noise, and they are adjusted accordingly.

Lastly, the condition regarding the pseudorapidity is motivated by the detector. For the resolved and superboosted reconstruction, $|\eta| < 2.5$, as this corresponds with the coverage of the inner detector. The boosted reconstruction demands a smaller condition, $|\eta| < 2$ because very large jets can end up at the edge of the detector, beyond the tracker.

A major part of the Higgs boson reconstruction studies is to decide whether a given event has b-jets in it, as the Higgs decays into a b-quark pair in this channel. Essentially, an event has the correct jets if it passes its respective delta-R condition, which depends on the reconstruction, and it is a b-jet when the jet contains a b-hadron, as a result of the hadronisation of the b-quarks.

In the boosted and superboosted reconstructions this is a straightforward task, because there is only one small/large-R jet, but in the resolved case it is a bit more subtle. The major difference is that the resolved reconstruction contains 2 jets and 2 or 3 jet candidates, so there is some combinatorics involved to check the various delta-R requirements. This is no more difficult, but it does take longer to run.

For a complete overview, the delta-R conditions mentioned earlier have also been included in table 1.

Table 1: This table shows explicitly the conditions used in the truth jet analysis algorithm, with transverse momentum p_T, pseudorapidity η and vector boson W as in the Feynman diagram mentioned in section 2.2. Note the similarities between the resolved and thesuperboosted reconstructions. As explained before, it makes sense that these reconstructions have very similar conditions, all on the lower end of the energy spectrum in order to cover all events. The major difference is that the superboosted reconstruction checks events for one jet only, while the resolved conditions always demand two jets. The table is the same for the reco analysis if one removes the condition on the Jet p_T

Reconstruction	Resolved	Boosted	Superboosted
Number of jets	2 or 3 small jets	≥ 1 large jet	≥ 1 large jet
Jet p_T [GeV]	> 20	> 250	> 20
Vector boson p_T [GeV]	> 150	> 250	> 150 [9]
Jet $\|\eta\|$	< 2.5	< 2.0	< 2.5
Delta-R	< 0.4	< 1.0	< 0.4

[9] It is possible to take the cut at 150 GeV, although the threshold for most events in the superboosted reconstruction will be much higher, at around 600 GeV.

4.4 Analysis on reco level

The analysis on truth level allows for precise theoretical simulations of interactions. This way, a general study can be done to study the superboosted approach.
Another advantage is that it is not necessary to use algorithms to find the b-hadrons, as they are already known from the start. This gives an idea of the optimal physical accuracy that can be obtained, because there are no limitations from the b-tagging algorithms necessary when analysing experimental data.

A major shortcoming in this analysis is that it does not account for the presence of the detector and everything about the particles in the interaction is known, in particular, properties that cannot be accessed experimentally. Therefore, it is required to switch to another kind of analysis simulation, on *reconstructed level* or *reco* in short, to be able to make predictions for the experimental data.

The idea of analysis on reco level is the same as in the analysis on truth level, but there are differences in the objects used and in the event selection.

Instead of b-hadrons, VR track jets[10] from the *anti-k_t* algorithm are used. The b-jet candidates from the truth analysis are replaced by *signal jets*, which are small-R jets that are detected by the calorimeters and are required as the track jets do not capture the neutral particles in the detector. After the signal jets have been confirmed to satisfy the delta-R conditions with respect to the VR track jets, it is possible to use b-tagging on the signal jets to conclude whether they are valid b-jets. Essentially, this skips some of the steps done in the analysis on truth level, but the general structure of the analysis is similar.

For the properties of the jets themselves, table 1 remains unchanged. The conditions on the jet p_T are maintained from the analysis on truth level, but the vector boson momenta are used instead of the Higgs boson momenta, as the latter are impossible to measure. This does not change the results significantly, because they are equal at first order.

[10] As explained in section 3.3.1

5 Results

In this section the core of this research is given. First, a check on jet properties and reconstruction methods is done, where observations from relativistic kinematics are checked to be consistent with the analysis that is done later. The main goal of this first project was to learn the ROOT framework and apprehend the physics involved, but this section will, in addition, make some of the claims done in earlier sections more plausible. In particular, the claims made at the end of section 2.2 and in section 3.4.

Subsequently the truth simulation results are shown and explained and followed by the reco simulations, which additionally include the ATLAS detector response. These simulations could be directly compared with actual data.

The final section will concern reco simulations of background processes in order to estimate the signal sensitivity.

For legibility and continuity of reading, only some of the figures will be shown in this section, but they are all included in appendix B (figures 22 - 48) in more detail.

5.1 First checks on jet properties and reconstruction methods

In this section, a few simple properties that can be derived from relativistic kinematics are checked using the analysis as described in the previous section (section 4):

- *Jet universality* for all b-objects (quarks/hadrons/jets)
- *Jet behaviour* with respect to delta-R

In addition, the resolved and boosted reconstructions and their logical combinations will be studied briefly to confirm their expected properties and check which other logical combinations can be fruitful when the superboosted reconstruction is added to the discussion.

The study of the truth and reco simulations in the following subsections will be guided by these preliminaries.

5.1.1 Jet Universality

The idea of this study is to check whether the b-jets can be used as proxies to study the b-quarks, as information on the latter is unavailable in actual data.
Furthermore, b-hadrons will be included in this discussion as well, to check their behaviour compared to b-quarks and b-jets.

In order to demonstrate this, it suffices to calculate delta-R between these different b-objects. The combinations are symmetric, so there are only three possibilities, which are given below (figure 10). The first figure is shown in more detail in appendix B (figures 25 and 26).
In these figures, there is a clear relation that the number of events drops significantly as delta-R increases, as can be seen from the shape. For example, if delta-R is calculated between a quark and a hadron, it is known that the quarks hadronise and the hadrons tend to decay in similar directions, which results in the behavior shown in the figures.

It can also be seen that the b-hadrons and b-jets align, which makes sense as the b-hadrons in a b-jet typically carry a large fraction of the jet's momentum ($\sim$ 70% - 80%).

Moreover, the figures show *jet universality* in the sense that the b-jet approximates the outgoing b-quark and b-hadron directions.

This fact enables the possibility to do the analysis on b-jets instead of b-quarks, as the latter are unknown in actual data[11].

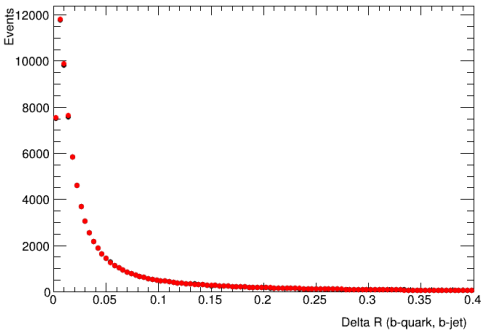

a) Delta-R of b-quark and b-jet.

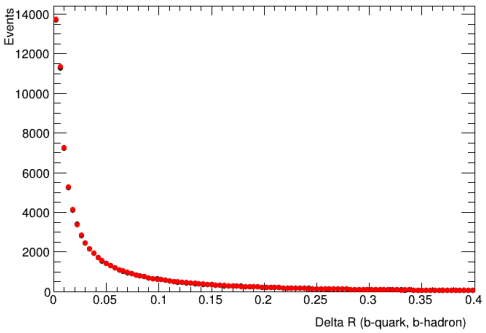

b) Delta-R of b-quark and b-hadron.

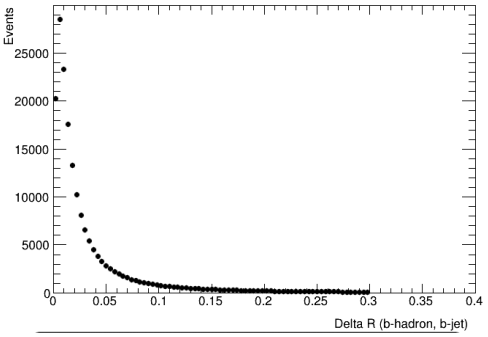

c) Delta-R of b-hadron and b-jet. There are no red dots as there are no quarks present here.

Figure 10: Number of events plotted as a function of delta-R between different b-objects. Red: anti b-quarks, Black b-quarks. The first figure has been given a more detailed display in appendix B (figures 25 and 26) as it is difficult to see both the red and black dots in the same figure. All other figures can be found in that appendix as well (22 to 26).

[11] Quarks are confined, so the b-quarks cannot be used in the analysis

5.1.2 Jet Behaviour

In the rest frame of the Higgs boson the decay always happens back-to-back, but if the Higgs boson has sufficient kinetic energy in the lab frame, the decay products become collimated, as known from relativistic kinematics. In particular, the jets start getting closer when the energy increases and eventually, if the energy is high enough, the jets will overlap. This is the main idea behind the resolved, boosted and superboosted reconstructions.

Calculating delta-R between two jets and plotting this histogram as a function of p_T^H, it is possible to show that the simulations are consistent with this jet behaviour.

The b-jets figure is shown below (figure 11). All other figures can be found in appendix B (figures 27 to 30).

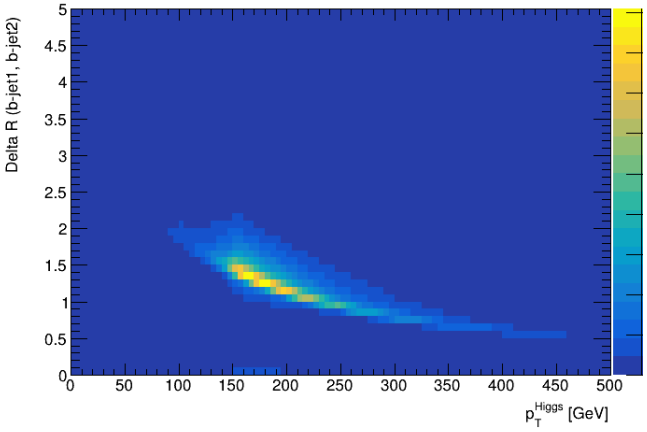

Figure 11: Delta-R of two b-jets plotted as a function of the Higgs p_T. The colour map indicates the expected number of events per bin, scaling linearly from 0 events (blue) to 909,6 (yellow). Total number of events: $7.320 \cdot 10^6$

The behaviour shown in figure 11 can be described by the following rule of thumb:

$$\Delta R(b,b) \sim \frac{2m_{Higgs}}{p_{T,Higgs}} \tag{5.1}$$

In figure 12 it is shown that this formula works quite well.

From formula 5.1, it is possible to estimate the values of p_T^H that define the optimal regions for resolved, boosted, and superboosted:

- Boosted at $p_T^H > 250$ GeV (delta-R < 1.0)
- Superboosted at $p_T^H > 600$ GeV (delta-R < 0.4)
- Resolved works best at lower energies, until the starting point of superboosted, i.e. $p_T^H < 600$ GeV, as the two jets get too close to be reconstructed individually.

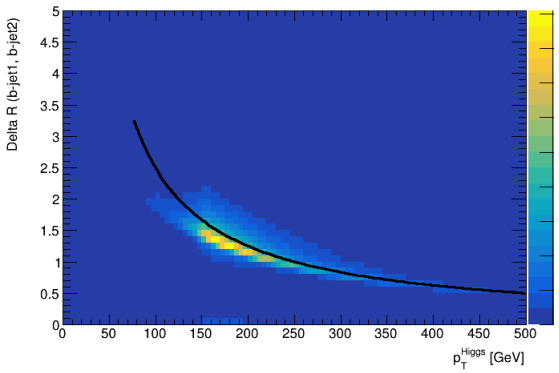

Figure 12: Delta-R of two b-jets plotted as a function of the Higgs p_T and in black the fit $\Delta R = 2m_{Higgs}/p_{T,Higgs}$. The colour map indicates the expected number of events per bin, scaling linearly from 0 events (blue) to 909,6 (yellow). Total number of events: $7.320 \cdot 10^6$

5.1.3 Reconstructions Characterisation

In order to check whether the analysis presented in this thesis is consistent with the claims on the expected behaviour of the resolved and boosted reconstructions, they need to be studied without the superboosted reconstruction. Another advantage of this approach is that the figures given in the following subsections will be easier to understand, as the presentation is the same.

The results are plotted as a function of the Higgs transverse momentum p_T^H, as this refers to the energy scales of the process. Subsequent plots will use the vector boson transverse momentum p_T^V, in this case the W boson, because the p_T^H is measured with much less precision. This is allowed as they are equal at first order.

In order to show the reconstructions behaviour at different energy scales, the results are plotted as a fraction of total events, where the events are only added to the total events if they pass one of the logical combinations shown in the figure. The adverb *only*[12] is used to exclude any possible overlap with other regimes and the reconstructions satisfy the properties as described in the experimental background section (section 3, table 1).

The results are shown in figure 13. This figure will be called the *characterisation figure* for future reference.

The observations that can be made from this plot are consistent with the expected behaviour of the resolved and boosted reconstructions.
At low energies ($p_T^H < 250$ GeV), the resolved technique works best, while at high energies ($p_T^H > 600$ GeV), the boosted technique is better.
Moreover, the overlap resolved & boosted is prominent in the region in between, as expected.

[12] In this plot this will be indicated by the logical symbol for AND ($\wedge$) and the logical negation ($\neg$). Following plots will instead use the adverb *only* as described in this paragraph.

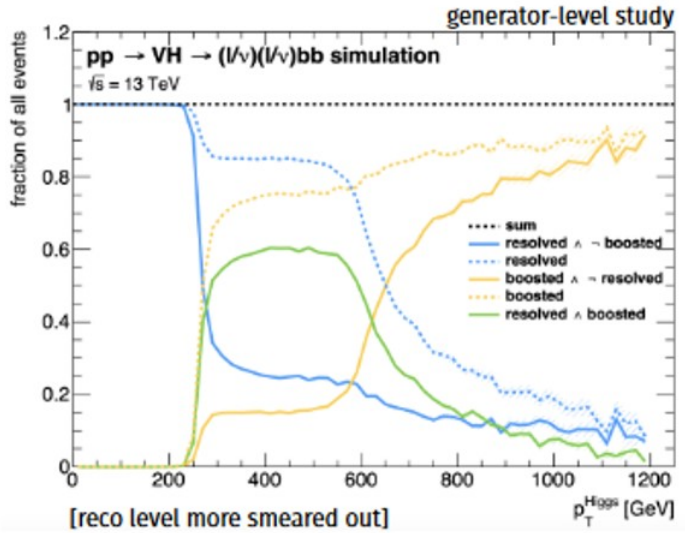

Figure 13: Fraction of total events that pass the conditions for a certain regime or logical combination of regimes. This figure gives insight in how the different reconstructions and their combinations perform at different p_T [6].

5.2 Truth Simulations

The necessary information has now been given to study the truth simulation results and to start investigating the superboosted reconstruction. As explained before, the results will be plotted using p_T^V instead of p_T^H, as the latter is measured with much less precision, but they are equal at first order.

Following this demonstration, the analysis will be taken one step higher to reco simulations.

Most figures and tables will not be displayed in the core text, but rather in appendix B.

5.2.1 Only Resolved – Superboosted– Only Boosted – Resolved & Boosted

The reconstruction characterisation figure (figure 13) hints at which logical combinations of reconstructions might be interesting to study. It seems wise to start with a general picture study and "zoom in" on interesting parts.

The following three logical combinations of reconstructions are considered to this end:

- Only resolved
- Only boosted
- Only resolved & only boosted

The combinations above are created using the resolved and boosted methods and are constructed such that they avoid the superboosted events, which is introduced in the next step:

- Superboosted (i.e. it can also include resolved and boosted events)

These combinations of reconstructions form a complete set, in the sense that they cover all possible events from any combination of resolved, boosted, and superboosted, and will not double-count events. This is illustrated using a Venn diagram, in figure 14a.

The histogram that is produced when the analysis is done on all events can been seen below, figure 14b. The expected number of events on the y-axis is put on a logarithmic scale.

From this figure, the following can be observed:

- There is a large overlap of resolved and boosted (excluding superboosted overlap) for p_T^V between 250 GeV and 600 GeV. This is consistent with the observation that the jets start overlapping at these energies.
- Superboosted covers more events than the other categories at $p_T^V > 600$ GeV. More precisely, the figure shows an efficiency, i.e. the number of events that can be reconstructed in a certain way, of about 70% for superboosted. This value agrees with the rule of thumb formula 5.1 (it predicts $p_T^V = 625$ GeV at $\Delta R = 0.4$).

It is insightful to consider the behaviour of the different reconstruction combinations with respect to each other instead of just the raw number of events. This is done by plotting the number of events as a fraction of the total number of events that has passed *one* of the reconstructions, called *passed events*.

The results are plotted in figure 15, in the same fashion as the characterisation figure.

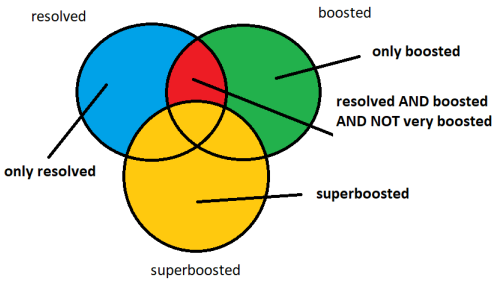

a) The Venn diagram

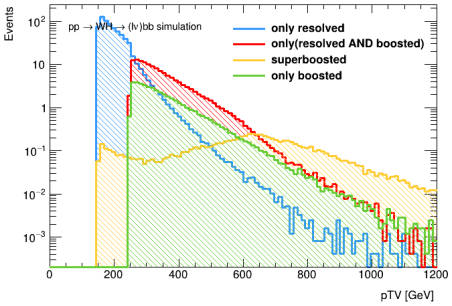

b) The total events figure

Figure 14: Reconstruction characterisation for only resolved, resolved & boosted, superboosted, only boosted. The total number of passed events is plotted as a function of p_T^V and a Venn diagram shows the logical structure of the different reconstruction combinations considered in this figure, with corresponding colours. The number of events in a certain energy interval is given in table 2

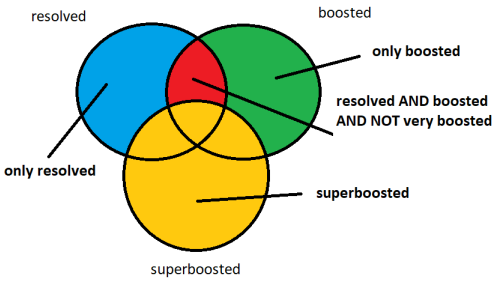

a) The Venn diagram

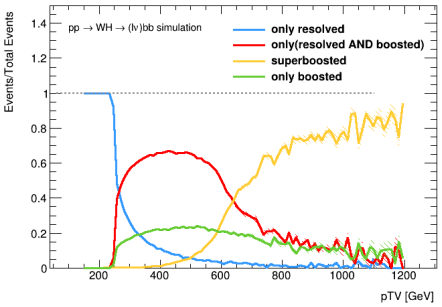

b) The fraction figure

Figure 15: Reconstruction characterisation for only resolved, resolved & boosted, superboosted, only boosted. The fraction of passed events to total events is plotted as a function of p_T^V and a Venn diagram shows the logical structure of the different reconstruction combinations considered in this figure, with corresponding colours.

5.2.2 Only Boosted - Only Superboosted– Overlap Boosted & Superboosted

Another region of interest is the high energy region or *tail* of the reconstructions, where it was unclear how the boosted and superboosted reconstructions are distributed.

The figures are given in figure 16 and in table 4.

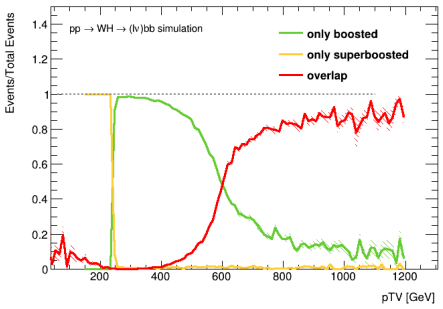

a) Fraction of passed events to total events.

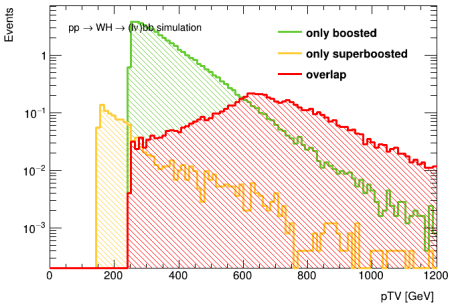

b) Total number of passed events.

Figure 16: Reconstruction characterisation for only boosted, only superboosted, overlap boosted & superboosted. The fraction of passed events to total events is plotted as a function of p_T^V. The number of events in a certain energy interval for figure b) is given in table 4.

First, note that near the tail of the reconstructions, the uncertainty increases and the figures become less smooth. This happens because there are much fewer events at high energy compared to low energy and is something to keep in mind in further discussions. To make this more quantitative: for $p_T^V < 600$ GeV, 99.638 % of events will be in this region (the low energy region) and for $p_T^V > 600$ GeV, 0.362 % will be in the high energy region.

This effect is a general feature of a falling p_T spectrum and is therefore the most prominent for the superboosted reconstruction.
Another observation that can be made is the small number of events that are reconstructed by the superboosted reconstruction at $p_T^V < 200$ GeV. This is impossible and most likely caused by a wrong truth-to-reco matching, which is delta-R based.

Regarding the analysis itself, it is now clear that the superboosted and overlap boosted/superboosted reconstructions are very similar. This means that the efficiency of the superboosted reconstruction is sufficient for the Higgs boson reconstruction.
Actually, from observing the small number of events that can only be reconstructed by the boosted analysis, it can be seen that about 5% of those events are missed by the superboosted reconstruction. The fact that the reconstructions are roughly matching is consistent with the large-R jets always being able to cover events that are also covered by small-R jets.

All other truth figures can be found in appendix B (figures 32 to 37), as well as the tables for the total events plots (tables 2 to 4).

5.2.3 Mass-cuts

As the Higgs mass is a known parameter, it is possible to add this to the event selection to reduce the fraction of events where the truth matching went wrong. The Higgs mass is ∼125 GeV, so only events that are sufficiently close to this value are accepted when applying these bounds, called *mass-cuts*. In this case, only events with a di-b-jet mass (2 b-jets) in bounds [80, 140] GeV are selected.

This procedure leads to similar results as before, without significant changes. It is interesting to note, however, that the mass-cuts do seem to reduce the 'local minima' behaviour as seen in the truth figures (e.g. in figure 14, the superboosted reconstruction shows a local minimum at low energy). This cut also removes the superboosted events at low p_T^V which confirms the suspicion that they are caused by a wrong truth-matching.

5.3 Reco Simulations

Guided by the conclusions of the analysis on truth level, it is now possible to do the same analysis on reco level, where the detector will be included in the simulation. As these reco results can be compared to the actual data, it is possible to draw conclusions on the efficiency of the superboosted reconstruction compared to the boosted reconstruction.

The results will be presented in the same fashion as was done in the analysis on truth level, so that they can be compared. However, only the differences will be highlighted, as those are the most interesting.

First, the general figures have to be discussed. For convenience, the truth and reco figures are shown side-to-side, figure 17.

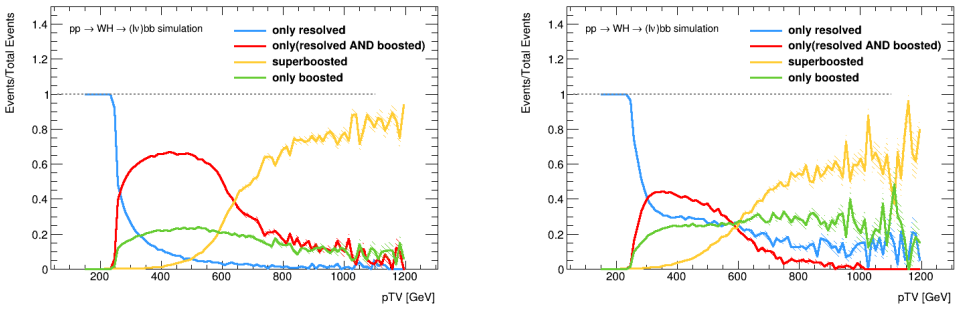

a) From truth simulations b) From reco simulations

Figure 17: Reconstruction characterisation for only resolved, resolved & boosted[13], superboosted, only boosted. The fraction of passed events to total events is plotted as a function of p_T^V. Left: truth. Right: reco

The figures are similar, but there are some differences:

- The uncertainties are higher on reco level. This comes from the fact that truth samples have more events than reco samples.
- Only boosted and only resolved do not drop as swiftly in the reco as in the truth simulations. At the same time, the overlap only resolved AND[14] only boosted covers a much tinier fraction of events. As this overlap is not the area of interest for superboosted, it can be ignored.

[13] As before, this is the overlap of only resolved and only boosted, c.f. 14a)
[14] This is a logical AND, not to be confused with the 'normal' and

- Superboosted at reco level covers a smaller fraction of events at high energy compared to at truth level.

In conclusion, the general behaviour and the 600 GeV 'switch' point seem to be consistent with the truth simulations. There are differences, but the only prominent difference would be the behaviour of the superboosted reconstruction at high p_T^V as it misses about 30% of only boosted events, compared to only 15% at truth level. This means that the efficiency of the superboosted reconstruction will be lower at reco level.

For completeness, all other results are given in appendix B (figures 38 to 43 and tables 5 to 7).

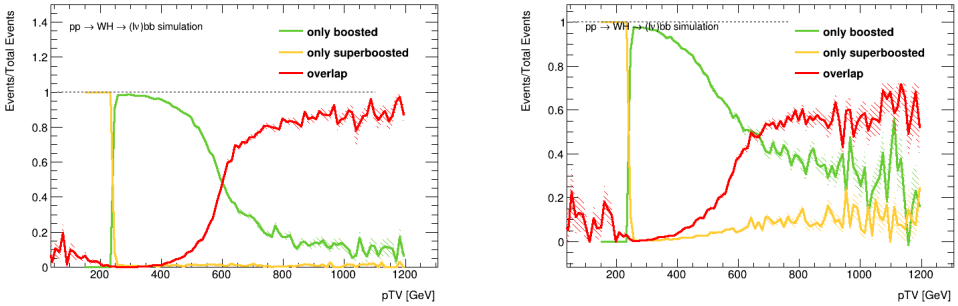

a) From truth simulations b) From reco simulations

Figure 18: Reconstruction characterisation for only resolved, resolved & boosted, superboosted, only boosted. The fraction of passed events to total events is plotted as a function of p_T^V. Left: truth. Right: reco. [15]

5.4 Backgrounds

In order to study the sensitivities of the reconstructions, the analysis now focuses on *background rejection*.
There exist various interactions that are similar to the $W \to \ell\nu$ $H \to b\bar{b}$ 1-lepton channel studied in this thesis, but should not be identified as such. Finding this correct *signal* while rejecting similar, but wrong signals (the *background*), is called background rejection. The main backgrounds, top quark pair ($t\bar{t}$) and W+ jets production are shown in figures 49 and 50 of appendix C.

The *significance*, in units of standard deviations, is then calculated as

$$Z = \frac{s}{\sqrt{s+b}} \tag{5.2}$$

where s is the signal and b is the background, using all events in the window between 100 GeV and 140 GeV, which is close to the Higgs mass ∼125 GeV [21].

[15] There is some strange behaviour in this plot's lay-out. The source of this error is unclear, but it does not invalidate the results shown.

Going through the analysis and applying the event selection cuts discussed in section 4, will produce the histograms given below (figures 19 and 20). These histograms show the number of events passed per bin of 10 GeV as a function of the Higgs candidate mass (i.e. 2 small-R jets for resolved, 1 large-R jet for boosted and 1 small-R jet for superboosted). The analysis with is done from a certain p_T^V onwards, in this case 400 GeV and 800 GeV.
The figures for $p_T^V > 500$, $p_T^V > 600$ and $p_T^V > 700$ can be found in appendix B (44 to 48).

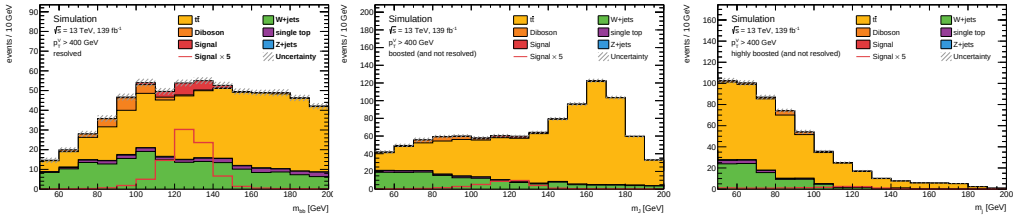

a) Resolved
Z = 0.984

b) Boosted
Z = 0.332

c) Superboosted
Z = 0.158

Figure 19: Background rejection for resolved, boosted and superboosted at $p_T^V > 400$ GeV. The significance Z is given as $s/\sqrt{s+b}$ where s is the signal and b is the background and is calculated using all events in the window between 100 GeV and 140 GeV.

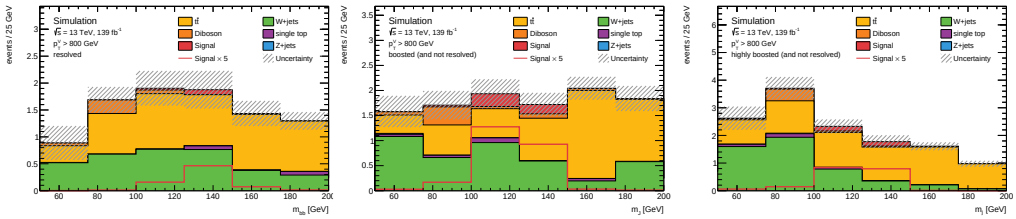

a) Resolved
Z = 0.0640

b) Boosted
Z = 0.230

c) Superboosted
Z = 0.161

Figure 20: Background rejection for resolved, boosted and superboosted at $p_T^V > 800$ GeV. The sensitivity Z is given as $s/\sqrt{s+b}$ where s is the signal and b is the background and is calculated using all events in the window between 100 GeV and 140 GeV.

The figures show stacked plots, where the different colours indicate contributions from the different backgrounds and in red the signal. This signal is also shown multiplied by a factor of 5 (the red line), making it easier to see on the figure.

The signal peaks around the Higgs mass of ∼125 GeV, which is a good sign.
The sensitivity trends are consistent with the expected behaviour of the reconstructions; it can be seen that resolved has a very high sensitivity at 400 GeV, but performs rather poorly at 800 GeV, where boosted and superboosted are better.

As the boosted and superboosted histograms do not include the overlap with resolved, it is possible to compare the significances of these two reconstructions.
At best, which is at 800 GeV, it is derived that the superboosted reconstruction is about 70% as sensitive as the boosted reconstruction.

6 Conclusion and Discussion

Different reconstruction techniques for Higgs bosons decaying to b-quark pairs have been studied in this thesis. The boosted and superboosted reconstructions at high energy were compared in order to draw conclusions on the performance of a new resolved and superboosted method compared to the existing resolved and boosted strategy.

The reco simulations show that the efficiency of the superboosted reconstruction at $p_T^V > 600$ GeV is about 30% worse compared to the boosted reconstruction. This means that about 30% of the events can only be reconstructed by the boosted method at these energies.

By studying the background rejections it is possible to draw conclusions on the sensitivity of the reconstruction techniques. From these results, it is clear that there is a trend of increasing sensitivity, as the energy increases, for the superboosted reconstruction. The best result is obtained at the highest energy considered, $p_T^V > 800$ GeV, where the superboosted sensitivity is about 70% as good as the boosted sensitivity.

These results suggest that without further optimisation of the background rejection, the considered resolved and superboosted reconstruction does not match the efficiency nor sensitivity of the resolved and boosted strategy yet.

With the recent and coming upgrades to the LHC, the pp collision data set will increase by nearly a factor 20. This allows to study even higher energy Higgs bosons, which are more uncommon to be produced. Therefore, it is interesting to optimise the superboosted reconstruction further.

References

[1] The ATLAS Collaboration. "Observation of a new particle in the search for the Standard Model Higgs boson with the ATLAS detector at the LHC". In: *Physics Letters B* 716.1 (2012), pp. 1–29. ISSN: 0370-2693. DOI: 10.1016/j.physletb.2012.08.020. URL: http://dx.doi.org/10.1016/j.physletb.2012.08.020.

[2] The CMS Collaboration. "Observation of a new boson at a mass of 125 GeV with the CMS experiment at the LHC". In: *Physics Letters B* 716.1 (2012), pp. 30–61. ISSN: 0370-2693. DOI: 10.1016/j.physletb.2012.08.021. URL: http://dx.doi.org/10.1016/j.physletb.2012.08.021.

[3] David J Griffiths. *Introduction to elementary particles; 2nd rev. version*. Physics textbook. New York, NY: Wiley, 2008.

[4] Mark Thomson. *Modern Particle Physics*. Cambridge University Press, 2013. DOI: 10.1017/CBO9781139525367.

[5] MissMJ-Own work by uploader, PBS NOVA, Fermilab, Office of Science, United States Department of Energy, Particle Data Group. *Particle content of the Standard Model. Courtesy to Wikipedia: 'Standard Model of Elementary Particles'*. https://www.researchgate.net/figure/Particle-content-of-the-Standard-Model-Courtesy-to-Wikipedia-Standard-Model-of_fig1_322568259. 2021.

[6] B. Moser. *The Beauty and the Boost: A Higgs boson tale*. https://indico.iihe.ac.be/event/1340/attachments/1860/2190/BrianMoser_BoostedVHbbATLAS_IIHESeminar.pdf. 2020.

[7] M. Tanabashi et al. (Particle Data Group). "Status of Higgs Boson Physics". In: *Phys. Rev. D 98, 030001 (2018)* (2019 update).

[8] The ATLAS Collaboration. "Measurements of WH and ZH production in the $H \to b\bar{b}$ decay channel in pp collisions at 13 TeV with the ATLAS detector". In: *Eur. Phys. J. C* 81.2 (2021), p. 178. DOI: 10.1140/epjc/s10052-020-08677-2. arXiv: 2007.02873 [hep-ex].

[9] ATLAS Collaboration. "Measurement of the associated production of a Higgs boson decaying into b-quarks with a vector boson at high transverse momentum in pp collisions at $s = 13$ TeV with the ATLAS detector". In: *Physics Letters B* 816 (2021), p. 136204. DOI: 10.1016/j.physletb.2021.136204. URL: https://doi.org/10.1016%2Fj.physletb.2021.136204.

[10] Lyndon Evans and Philip Bryant. "LHC Machine". In: *Journal of Instrumentation* 3.08 (2008), S08001–S08001. DOI: 10.1088/1748-0221/3/08/s08001. URL: https://doi.org/10.1088/1748-0221/3/08/s08001.

[11] The ATLAS Collaboration. "The ATLAS Experiment at the CERN Large Hadron Collider". In: *Journal of Instrumentation* 3.08 (2008), S08003–S08003. DOI: 10.1088/1748-0221/3/08/s08003. URL: https://doi.org/10.1088/1748-0221/3/08/s08003.

[12] S. Chatrchyan et al. "The CMS Experiment at the CERN LHC". In: *JINST* 3 (2008), S08004. DOI: 10.1088/1748-0221/3/08/S08004.

[13] K. Aamodt et al. "The ALICE experiment at the CERN LHC". In: *JINST* 3 (2008), S08002. DOI: 10.1088/1748-0221/3/08/S08002.

[14] A. Augusto Alves Jr. et al. "The LHCb Detector at the LHC". In: *JINST* 3 (2008), S08005. DOI: 10.1088/1748-0221/3/08/S08005.

[15] Nguyen Ky and Nguyễn Vân. "Was the Higgs Boson Discovered?" In: *Communications in Physics* 25 (Mar. 2015). DOI: 10.15625/0868-3166/25/1/5941.

[16] Matteo Cacciari, Gavin P Salam, and Gregory Soyez. "The anti-ktjet clustering algorithm". In: *Journal of High Energy Physics* 2008.04 (2008), pp. 063–063. ISSN: 1029-8479. DOI: 10.1088/1126-6708/2008/04/063. URL: http://dx.doi.org/10.1088/1126-6708/2008/04/063.

[17] The ATLAS Collaboration. "Search for the Standard Model Higgs boson produced in association with a vector boson and decaying to a b-quark pair with the ATLAS detector". In: *Physics Letters B* 718.2 (2012), pp. 369–390. ISSN: 0370-2693. DOI: 10.1016/j.physletb.2012.10.061. URL: http://dx.doi.org/10.1016/j.physletb.2012.10.061.

[18] ROOT. *Python interface: PyROOT*. https://root.cern/manual/python/. 2021.

[19] Rene Brun and Fons Rademakers. "ROOT - An Object Oriented Data Analysis Framework". In: *AIHENP'96 Workshop, Lausane*. Vol. 389. 1996, pp. 81–86.

[20] D. Piparo. *The ROOT's Notebook interface and the SWAN Service*. https://indico.cern.ch/event/579588/contributions/2356053/attachments/1364606/2066555/JupyterAndSWAN_ALICE_021116.pdf. 2017.

[21] Glen Cowan et al. "Asymptotic formulae for likelihood-based tests of new physics". In: *The European Physical Journal C* 71.2 (2011). DOI: 10.1140/epjc/s10052-011-1554-0. URL: https://doi.org/10.1140%2Fepjc%2Fs10052-011-1554-0.

[22] L. D. Landau and E. M. Lifshitz. *Statistical Physics Part I*. 3rd. Amsterdam: Elsevier, 1980.

[23] Brian Moser. "The Beauty and the Boost: a Higgs Boson Tale - Measurements of Higgs Boson Production at High Energy in Decays to Bottom Quarks and Their Interpretations with the ATLAS Experiment at the LHC". Presented 04 Mar 2022. 2021. URL: https://cds.cern.ch/record/2803776.

Appendix A. The Higgs Mechanism

The following derivation is based on D. J. Griffith's Introduction to Elementary Particles and M. Thomson's Modern Particle Physics, see [3, 4].
First, the demonstration as given in the thesis, section 2.3, will be repeated.
Afterwards, this will be expanded upon to both a complex valued Lagrangian and the idea of gauge transformations.

Symmetry Breaking

In order to understand the Higgs Mechanism, it is crucial to first look at a concept called *Symmetry Breaking*.

Suppose ϕ is a scalar (spin-0) field with potential

$$V(\phi) = \frac{1}{2}\mu^2\phi^2 + \frac{1}{4}\lambda\phi^4 \tag{6.1}$$

Then the *Lagrangian* of this theory becomes[16]

$$\mathcal{L} = \frac{1}{2}(\partial_\mu\phi)(\partial^\mu\phi) - V(\phi) \tag{6.2}$$

Where $\frac{1}{2}(\partial_\mu\phi)(\partial^\mu\phi)$ is the kinetic term, μ^2 can be interpreted as a square of a mass term, and λ is related to the (self-) interaction strength.

As can be seen in plot 6, the shape of the potential depends on the sign of μ^2.
In the case $\mu^2 > 0$, the potential has a minimum at $\phi = 0$ and we conclude that the Lagrangian describes a spin-0 particle with mass μ. The interesting case is when $\mu^2 < 0$, because then there is a minimum, called the *vacuum expectation value* obtained from setting $\frac{dV(\phi)}{d\phi} = 0$:

$$\phi \equiv \pm v = \pm\sqrt{\frac{-\mu^2}{\lambda}} \tag{6.3}$$

Without loss of generality, ϕ can be expanded around v i.e. $\phi = v + \eta$ for some perturbation η. Then the Lagrangian (6.2) becomes, using (6.3):

$$\begin{aligned}
\mathcal{L}(\eta) &= \frac{1}{2}(\partial_\mu\eta)(\partial^\mu\eta) - V(\eta) \\
&= \frac{1}{2}(\partial_\mu\eta)(\partial^\mu\eta) - \frac{1}{2}\mu^2(v+\eta)^2 - \frac{1}{4}\lambda(v+\eta)^4 \\
&= \frac{1}{2}(\partial_\mu\eta)(\partial^\mu\eta) - \lambda v^2\eta^2 - \lambda v\eta^3 - \frac{1}{4}\lambda\eta^4 + \frac{1}{4}\lambda v^4
\end{aligned} \tag{6.4}$$

where the last term is a constant and might as well be ignored in the Lagrangian.

This new Lagrangian can be compared one-to-one with (6.2), if it is written in the following form:

$$\mathcal{L}(\eta) = \frac{1}{2}(\partial_\mu\eta)(\partial^\mu\eta) - \frac{1}{2}m_\eta^2\eta^2 - V(\eta) \tag{6.5}$$

with $m_\eta^2 = 2\lambda v^2 = -2\mu^2$ a a square of a mass term, and $V(\eta) = \lambda v\eta^3 + \frac{1}{4}\lambda\eta^4$ a potential term.

[16] Summation over $\mu = 0, 1, 2, 3$ implied, mostly-minuses convention

The original Lagrangian had a potential term with a vacuum expectation value minimum which could be expanded around, breaking the symmetry of the Lagrangian. By some clever manipulations and one-to-one comparison, this symmetry broken Lagrangian introduces a new mass term m_η and a potential $V(\eta)$ term, including a new triple interaction. Although a relatively simple calculation, it lies at the foundation of the full Higgs Mechanism, and the idea remains the same throughout all derivations.

Moreover, it is interesting to note the similarities between the Higgs symmetry breaking and the symmetry breaking encountered when discussing phase transitions in statistical mechanics. A particularly clarifying demonstration of this phenomenon can be found in a book by it's discoverer L. D. Landau and E. M. Lifshitz [22].

It gets more complex

In order to understand the Higgs Mechanism, the next step should be to expand the symmetry breaking discussed in the former paragraph to a symmetry breaking of a complex scalar field.
To this goal, let us write ϕ explicitly as a real and imaginary component:

$$\phi = \frac{1}{\sqrt{2}}(\phi_1 + i\phi_2) \tag{6.6}$$

with Langrangian

$$\mathcal{L} = (\partial_\mu \phi)^*(\partial^\mu \phi) - V(\phi) \tag{6.7}$$

where $V(\phi) = \mu^2\phi^*\phi + \lambda(\phi^*\phi)^2$ and * indicates complex conjugation. This $V(\phi)$ is the famous *Mexican Hat potential*, plotted in figure 21.

Plug in the definition of ϕ in its components, and one derives straightforwardly

$$\mathcal{L} = \frac{1}{2}(\partial_\mu\phi_1)(\partial^\mu\phi_2) + \frac{1}{2}(\partial_\mu\phi_2)(\partial^\mu\phi_2) - \frac{1}{2}\mu^2(\phi_1^2 + \phi_2^2) - \frac{1}{4}\lambda(\phi_1^2 + \phi_2^2)^2 \tag{6.8}$$

Again, in a similar sense as before, there exists a minimum for μ^2. Though in this case it is an infinite set of minima defined by

$$\phi_1^2 + \phi_2^2 \equiv v^2 = \frac{-\mu^2}{\lambda} \tag{6.9}$$

The Lagrangian can again be expanded around this vacuum expectation value. Without loss of generality, expand only ϕ_1 around v and with the commonly used notation in the literature, the field components are expanded as

$$\phi_1 = v + \eta \text{ and } \phi_2 = \xi \tag{6.10}$$

From which follows the Lagrangian

$$\mathcal{L} = \frac{1}{2}(\partial_\mu\eta)(\partial^\mu\eta) + \frac{1}{2}(\partial_\mu\xi)(\partial^\mu\xi) - V(\eta,\xi) \tag{6.11}$$

and

$$\begin{aligned} V(\eta,\xi) &= \frac{1}{2}\mu^2\left[(v+\eta)^2 + \xi^2\right] + \frac{1}{4}\lambda\left[(v+\eta^2) + \xi^2\right]^2 \\ &= -\frac{1}{4}\lambda v^4 + \lambda v^2\eta^2 + \lambda v\eta^3 + \frac{1}{4}\lambda\eta^4 + \frac{1}{4}\lambda\xi^4 + \lambda v\eta\xi^2 + \frac{1}{2}\lambda\eta^2\xi^2 \end{aligned} \tag{6.12}$$

where $\mu^2 = -\lambda v^2$ is used, as before.

This Langrangian is rather messy, so it is better to write in the following form, introducing again a mass term m_η

$$\mathcal{L} = \frac{1}{2}(\partial_\mu \xi)(\partial^\mu \xi) + \frac{1}{2}(\partial_\mu \eta)(\partial^\mu \eta) - \frac{1}{2} m_\eta^2 \eta^2 - V_{int}(\eta, \xi) \tag{6.13}$$

with the interaction terms combined into V_{int}

From this Lagrangian (6.13) it is immediately obvious that we have a massive scalar η field and a *massless* scalar ξ field as a consequence of the symmetry breaking. The particles (excitations) of this last field are called *Goldstone bosons*, that appear when a continuous symmetry is spontaneously broken, like in the Higgs Mechanism. In this thesis the notion of Goldstone bosons will not be expanded upon. In fact, it is not required to this discuss this, for we will see shortly that the Goldstone bosons can be eliminated from the theory by using a certain *gauge transformation*.

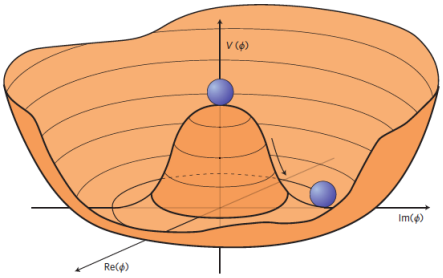

Figure 21: Plot of the so-called *Mexican Hat potential* for the potential of the Higgs field given by $V(\phi) = \mu^2\phi^*\phi + \lambda(\phi^*\phi)^2$ and $\mu^2 < 0$. In this plot, $Re(\phi)$ indicates the real part of ϕ and $Im(\phi)$ indicates the imaginary part of ϕ. In the text above these were mentioned as ϕ_1 and ϕ_2 respectively. From https://cds.cern.ch/record/1638469/plots

Gauge Transformations

In a general sense, gauge transformations are a very difficult mathematical concept. Luckily we can restrict ourselves to concrete examples and applications to the Higgs Mechanism at a much more accessible level.

To illustrate what a gauge transformation is, consider the following example.
Take the magnetic field $\mathbf{B}$ and the vector potential $\mathbf{A}$, such that $\mathbf{B} = \nabla \times \mathbf{A}$.
However, consider now $\mathbf{A} \to \mathbf{A}' = \mathbf{A} + \nabla\chi$, with χ a differentiable scalar field. Then **A'** is also a solution to **B**:

$$\begin{aligned} \mathbf{B} &= \nabla \times \mathbf{A'} \\ &= \nabla \times (\mathbf{A} + \nabla\chi) \\ &= \nabla \times \mathbf{A} + \nabla \times (\nabla\chi) \\ &= \nabla \times \mathbf{A} \end{aligned} \tag{6.14}$$

This can be applied to the symmetry breaking for a complex scalar field. In this case, A is called *gauge invariant* and $A \to A'$ is called a *gauge transformation* with *gauge* χ. Back to the Higgs Mechanism, observe that the gauge transformation $\phi \to \phi' = e^{i\alpha}\phi$ leaves (6.8) invariant. This is called a *global* U(1) symmetry[17].

Note however that ϕ does not satisfy a *local* U(1) symmetry:

$$\phi(x) \to \phi'(x) = e^{ig\chi(x)}\phi(x) \tag{6.15}$$

unless the derivatives transform as

$$\partial_\mu \to D_\mu = \partial_\mu + igB_\mu \tag{6.16}$$

for some gauge field B_μ for which $B\mu \to B'_\mu = B_\mu - \partial_\mu\chi(x)$

It is actually quite illustrative to demonstrate this proof. Suppose

$$\mathcal{L}' = (D'_\mu\phi')^*(D^{\mu\prime}\phi') - V(\phi'^2) \tag{6.17}$$

For $\phi^2 = \phi\phi^*$ it trivially follows that $V(\phi'^2)$ transforms accordingly. Then from the following identity the proof follows:

$$\partial_\mu(e^{-ig\chi}\phi) = -ig(\partial_\mu\chi)e^{-ig\chi}\phi + e^{-ig\chi}\partial_\mu\phi \tag{6.18}$$

Such that:

$$\begin{aligned}
\mathcal{L}' &= (D'_\mu\phi')^*(D^{\mu\prime}\phi') - V(\phi'^2) \\
&= (\partial_\mu - igB'_\mu)e^{-ig\chi}\phi(\partial^{\mu\prime} + igB^{\mu\prime})e^{ig\chi}\phi - V(\phi'^2) \\
&= (\partial_\mu - igB_\mu + ig\partial_\mu\chi)e^{-ig\chi}\phi(\partial^\mu + igB^\mu - ig\partial^\mu\chi)e^{ig\chi}\phi - V(\phi^2) \\
&= (\partial_\mu - ig\partial_\mu\chi - igB_\mu + ig\partial_\mu\chi)\phi(e^{-ig\chi}e^{ig\chi})(\partial^\mu + ig\partial^\mu\chi + igB^\mu - ig\partial^\mu\chi)\phi - V(\phi^2) \\
&= (\partial_\mu - igB_\mu)\phi(\partial^\mu + igB^\mu)\phi - V(\phi^2) \\
&= (D_\mu\phi)^*(D^\mu\phi) - V(\phi^2) = \mathcal{L}
\end{aligned} \tag{6.19}$$

The necessary preliminaries have now been laid out to study the Higgs Mechanism in full.

The Higgs Mechanism

If the gauge transformations are added to the complex valued Lagrangian (6.21) with potential $V(\phi) = \mu^2\phi^2 + \lambda\phi^4$, the final Lagrangian to be discussed is derived.
However, by introducing the gauge field B, there must also arise a kinetic and a mass term for B. Though by gauge invariance the mass term $\frac{1}{2}m_B B_\mu B^\mu$ cannot appear and actually only the kinetic term remains. For this gauge field is a spin-1 field[18], the kinetic term looks like

$$-\frac{1}{4}F_{\mu\nu}F^{\mu\nu} \tag{6.20}$$

[17] *Global* because α does not depend on space-time x, and U(1) is the *unitary group* of degree 1

[18] The proof of this statement and the following expression for the kinetic term will not be given in this thesis. Consider e.g. [3] to this end.

where $F^{\mu\nu} = \partial^\mu B^\nu - \partial^\nu B^\mu$
So that the Lagrangian becomes:

$$\begin{aligned}\mathcal{L} &= -\frac{1}{4}F_{\mu\nu}F^{\mu\nu} + (D_\mu\phi)^*(D^\mu\phi) - \mu^2\phi^2 - \lambda\phi^4 \\ &= -\frac{1}{4}F_{\mu\nu}F^{\mu\nu} + (\partial_\mu - igB_\mu)\phi^*(\partial^\mu + igB^\mu)\phi - \mu^2\phi^2 - \lambda\phi^4 \\ &= -\frac{1}{4}F_{\mu\nu}F^{\mu\nu} + (\partial_\mu\phi)^*(\partial^\mu\phi) - \mu^2\phi^2 - \lambda\phi^4 - igB_\mu\phi^*(\partial^\mu\phi) + ig(\partial_\mu\phi^*)B^\mu\phi + g^2B_\mu B^\mu\phi^*\phi\end{aligned} \tag{6.21}$$

Like before, expand around the vacuum expectation value:

$$\phi = \frac{1}{\sqrt{2}}(v + \eta + i\xi) \tag{6.22}$$

And substitute in the Lagrangian above to get the final result:

$$\mathcal{L} = \frac{1}{2}(\partial_\mu\eta)(\partial^\mu\eta) - \lambda v^2\eta^2 + \frac{1}{2}(\partial_\mu\xi)(\partial^\mu\xi) - \frac{1}{4}F_{\mu\nu}F^{\mu\nu} + \frac{1}{2}g^2v^2B_\mu B^\mu + gvB_\mu(\partial^\mu\xi) - V_{int} \tag{6.23}$$

The first 2 terms can be associated with the massive η field, the 3th term with the massless Goldstone ξ field and the $\frac{1}{2}g^2v^2B_\mu B^\mu$ term can be identified as a mass term for the B field (with kinetic term as before), which originally was assumed *massless*. This is truly the Higgs Mechanism in action. The Lagrangian (6.23) is physically completely equivalent to the original Lagrangian (6.21). However, by spontaneously breaking the symmetry of this Lagrangian, the local U(1) symmetry forces a gauge field to become massive. It is not strange to imagine that e.g. the W and Z fields in the Standard Model acquire their masses through this mechanism.
V_{int} just gathers all interaction terms, except for one which is explicitly left out of this interaction potential:

$$gvB_\mu(\partial^\mu\xi) \tag{6.24}$$

This is a potentially harmful term, as it describes an interaction where the spin-0 ξ field turns into a spin-1 B field. Luckily, the Goldstone field can be eliminated from the Lagrangian altogether.

Making the gauge transformation

$$B_\mu \to B'_\mu = B_\mu + \frac{1}{gv}\partial_\mu\xi \tag{6.25}$$

And collecting the terms associated with ξ in the following way:

$$\frac{1}{2}(\partial_\mu\xi)(\partial^\mu\xi) + (\partial^\mu\xi) + \frac{1}{2}g^2v^2B_\mu B^\mu = \frac{1}{2}g^2v^2\left(B_\mu + \frac{1}{gv}(\partial_\mu\xi)\right)^2 \tag{6.26}$$

The Lagrangian becomes

$$\mathcal{L} = \frac{1}{2}(\partial_\mu\eta)(\partial^\mu) - \lambda v^2\eta^2 - \frac{1}{4}F_{\mu\nu}F^{\mu\nu} + \frac{1}{2}g^2v^2B'_\mu B^{\mu\prime} - V_{int} \tag{6.27}$$

Therefore, choosing the correct gauge $\chi = -\frac{\xi}{gv}$, the Goldstone field ξ vanishes from the Lagrangian. This gauge is called the *Unitary gauge*.

Substituting this gauge in the definition of ϕ:

$$\phi \to \phi' = \exp\left(-\frac{i\xi}{v}\right)\phi \tag{6.28}$$

This expression can be used to derive an important characteristic of the Higgs field. To this end, expand up to first order the fields η and ξ in the expression for the vacuum expectation value expansion (6.22):

$$\begin{aligned}\phi &= \frac{1}{\sqrt{2}}(v+\eta+i\xi) \\ &= \frac{1}{\sqrt{2}}(v+\eta+i\xi+i\frac{\eta\xi}{v}) \text{ (to first order)} \\ &= \frac{1}{\sqrt{2}}((v+\eta)(1+\frac{i\xi}{v})) \\ &= \frac{1}{\sqrt{2}}(v+\eta)\exp\left(\frac{i\xi}{v}\right) \text{ (to first order)}\end{aligned} \tag{6.29}$$

Substituting this result in (6.28)

$$\begin{aligned}\phi \to \phi' &= \frac{1}{\sqrt{2}}\exp\left(\frac{-i\xi}{v}\right)(v+\eta)\exp\left(\frac{i\xi}{v}\right) \\ &= \frac{1}{\sqrt{2}}(v+\eta) \\ &\equiv \frac{1}{\sqrt{2}}(v+h)\end{aligned} \tag{6.30}$$

where η is usually written explicitly as the *Higgs field* h in the literature.

From here it is worthwhile to express the Lagrangian (6.21) in its full glory, using this last result:

$$\begin{aligned}\mathcal{L} &= (\partial D_\mu\phi)^*(\partial D^\mu\phi) - \frac{1}{4}F_{\mu\nu}F^{\mu\nu} - \mu^2\phi^2 - \lambda\phi^4 \\ &= \frac{1}{2}(\partial_\mu - igB_\mu)(v+h)(\partial^\mu + igB^\mu)(v+h) - \frac{1}{4}F_{\mu\nu}F^{\mu\nu} - \frac{1}{2}\mu^2(v+h)^2 - \frac{1}{4}\lambda(v+h)^4 \\ &= \frac{1}{2}(\partial_\mu h)(\partial^\mu h) + \frac{1}{2}g^2B_\mu B^\mu(v+h)^2 - \frac{1}{4}F_{\mu\nu}F^{\mu\nu} - \lambda v^2h^2 - \lambda vh^3 - \frac{1}{4}\lambda h^4 + \frac{1}{4}\lambda v^4 \\ &= \frac{1}{2}(\partial_\mu h)(\partial^\mu h) - \lambda v^2h^2 - \frac{1}{4}F_{\mu\nu}F^{\mu\nu} + \frac{1}{2}g^2v^2B_\mu B^\mu + g^2vB_\mu B^\mu h + \frac{1}{2}g^2B_\mu B^\mu h^2 - \lambda vh^3 - \frac{1}{4}\lambda h^4\end{aligned} \tag{6.31}$$

In this final expression for the Lagrangian of the Higgs field, the terms can be ordered in four groups of two. The first two terms arise from the massive h scalar. The second group describe the massive gauge boson B, which initially was assumed massless. The third group contains interactions between h and B, and the last two terms describe self-interactions of the Higgs field.
In particular, from this equation, the Higgs boson mass $m_H = \sqrt{2\lambda}v$ and the gauge boson mass $m_B = gv$ are immediately read off. This concludes the discussion of the theoretical background of the Higgs boson. It remains however to investigate the specific decay mode used in the jet analysis of this thesis, and to describe the analysis methods in more detail.

Appendix B. Additional Figures

First Checks

1D delta-R plots

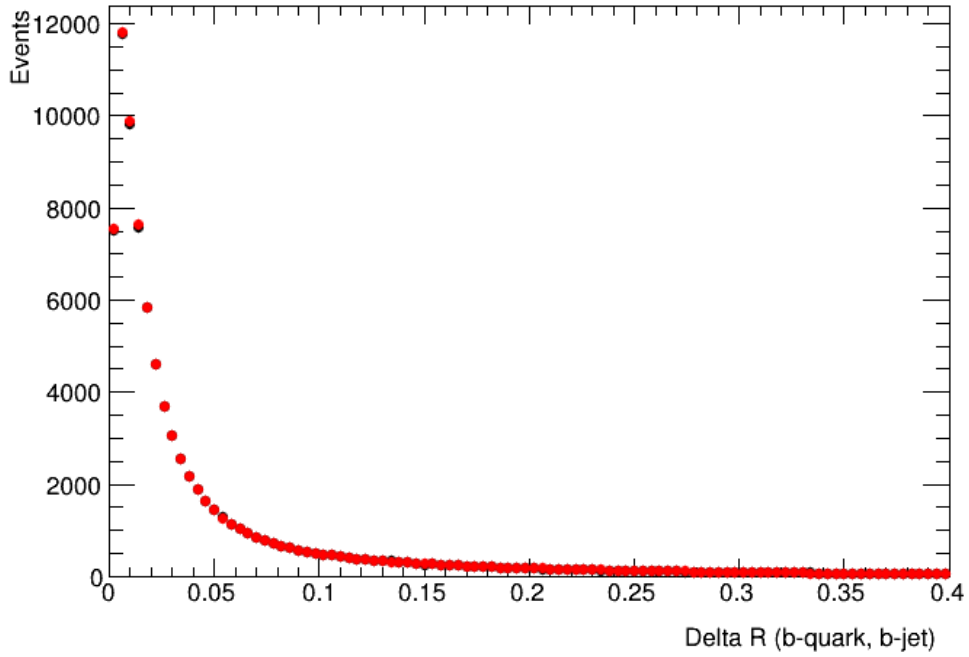

Figure 22: Delta-R of b-quark and b-jet.

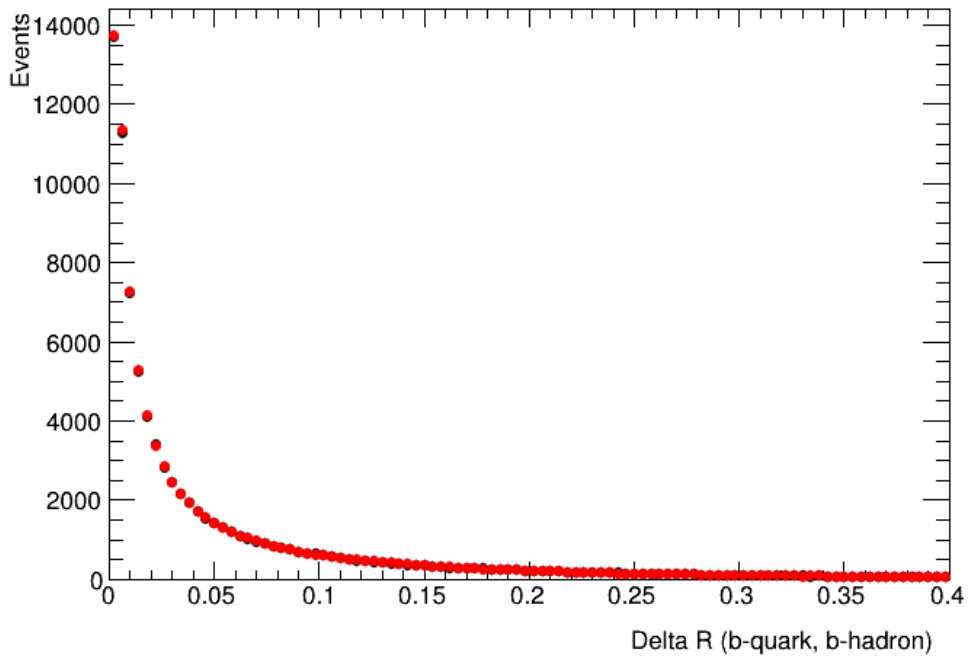

Figure 23: Delta-R of b-quark and b-hadron.

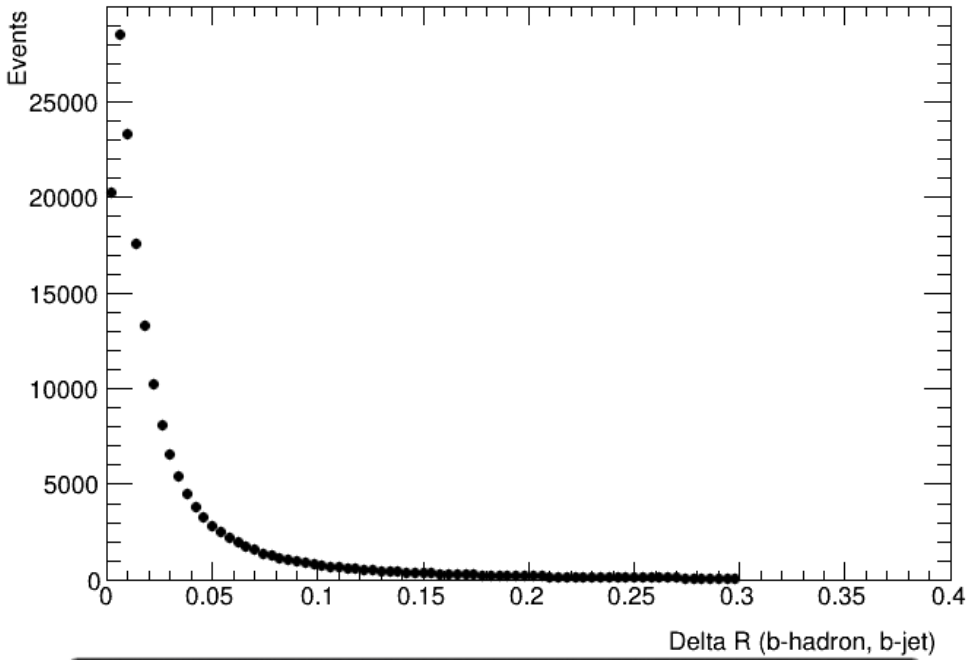

Figure 24: Delta-R of b-hadron and b-jet. There are no red dots as there are no quarks present here.

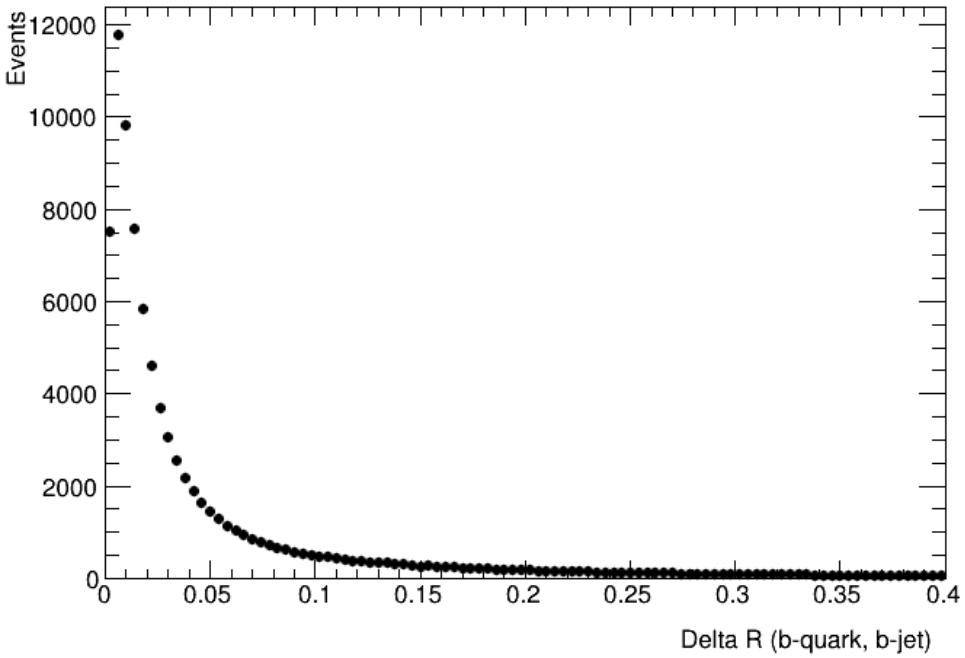

Figure 25: Delta-R of b-quark and b-jet. Only the b-quarks are displayed.

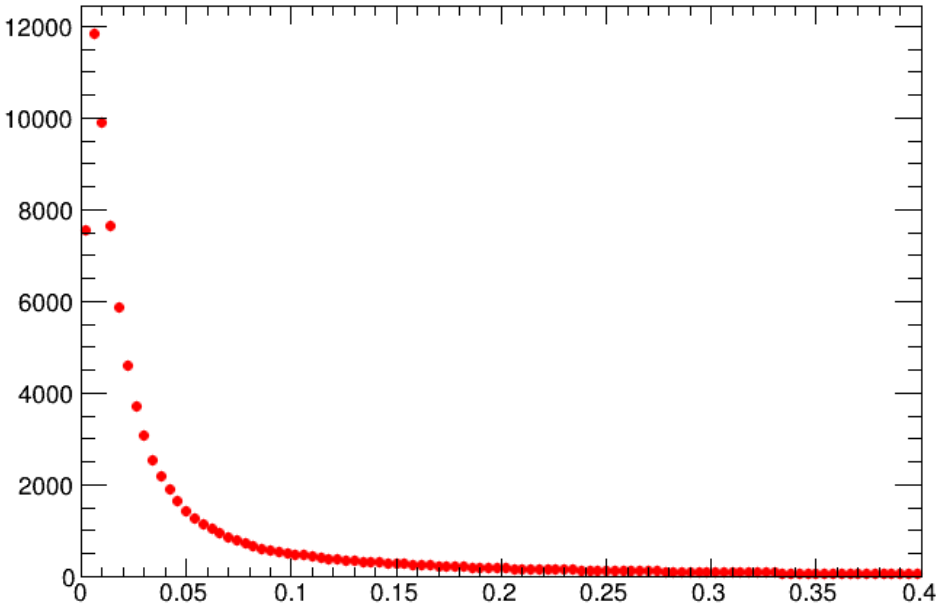

Figure 26: Delta-R of b-quark and b-hadron. Only the anti b-quarks are displayed.

2D delta-R plots

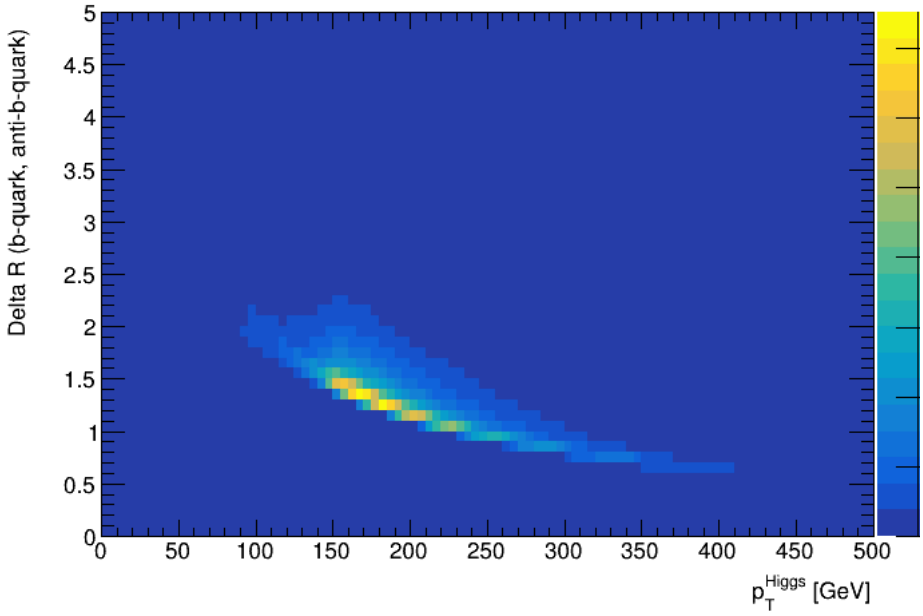

Figure 27: Delta-R of a b-quark pair plotted as a function of the Higgs p_T. The colour map indicates the expected number of events, scaling linearly from 0 events (blue) to 3760 (yellow). Total number of events: $7,3 \cdot 10^6$

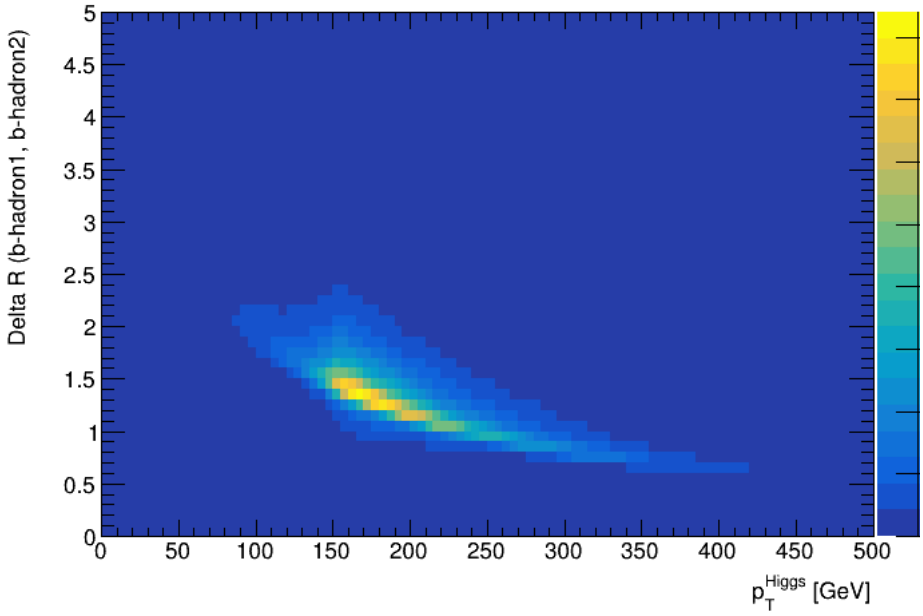

Figure 28: Delta-R of two b-hadrons plotted as a function of the Higgs p_T. The colour map indicates the expected number of events, scaling linearly from 0 events (blue) to 1679 (yellow). Total number of events: $7,3 \cdot 10^6$

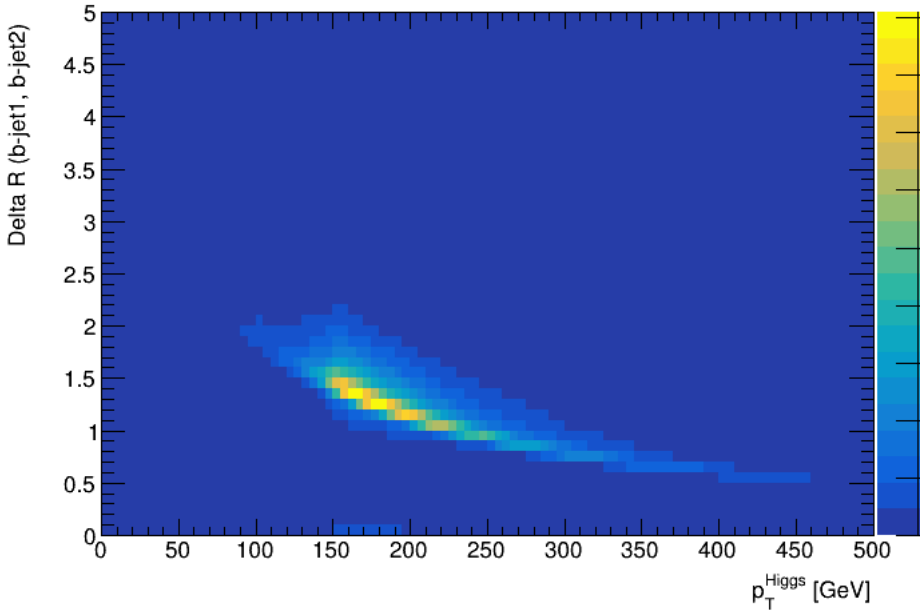

Figure 29: Delta-R of two b-jets plotted as a function of the Higgs p_T. The colour map indicates the expected number of events, scaling linearly from 0 events (blue) to 909,6 (yellow). Total number of events: $7,3 \cdot 10^6$

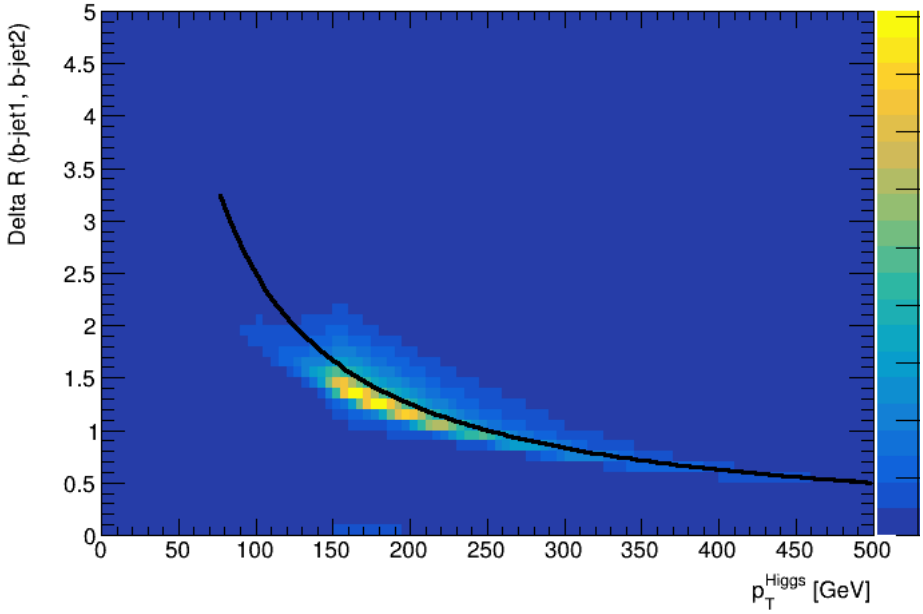

Figure 30: Delta-R of two b-jets plotted as a function of the Higgs p_T and in black the fit $\Delta R = 2m_{Higgs}/p_{T,Higgs}$. The colour map indicates the expected number of events, scaling linearly from 0 events (blue) to 909,6 (yellow). Total number of events: $7,3 \cdot 10^6$

Regimes Characterisation

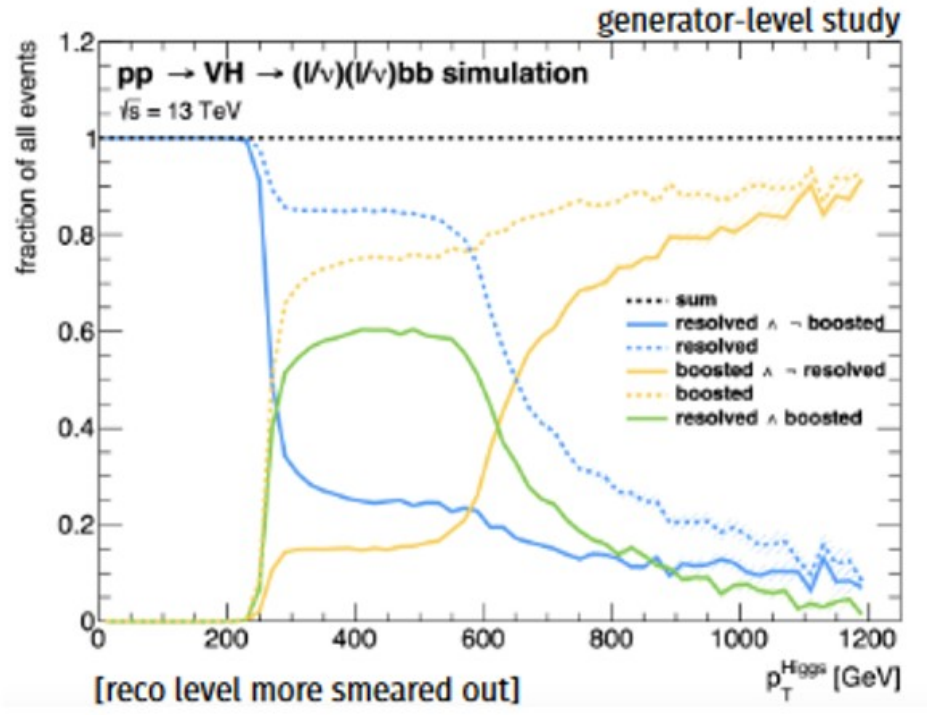

Figure 31: Fraction of total events that pass the conditions for a certain regime or logical combination of regimes. This figure gives insight in how the different reconstructions and their combinations perform at different p_T [6].

Truth Plots

Only Resolved – Superboosted– Only Boosted – Resolved & Boosted

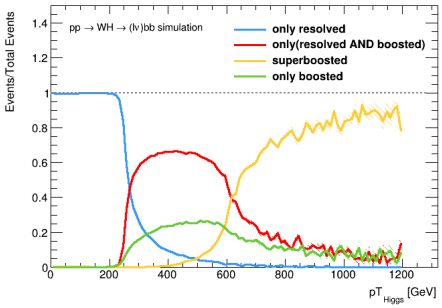

a) Fraction of passed events to total events.

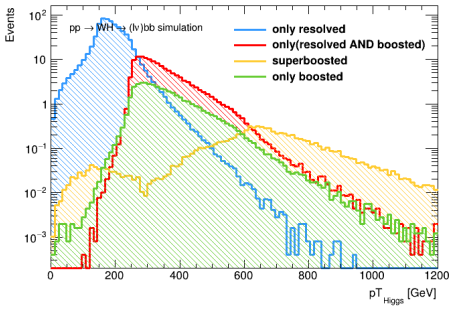

b) Total number of passed events.

Figure 32: Truth Reconstruction characterisations for only resolved, superboosted, only boosted, resolved & boosted. Plotted as functions of p_T^H.

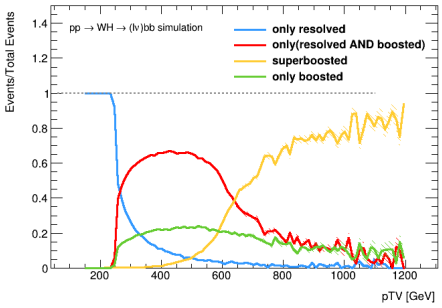

a) Fraction of passed events to total events.

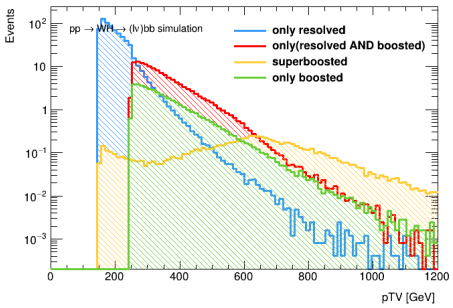

b) Total number of passed events.

Figure 33: Truth Reconstruction characterisations for only resolved, superboosted, only boosted, resolved & boosted. Plotted as functions of p_T^V. The number of events in a certain energy interval is given in table 2

Resolved – Superboosted

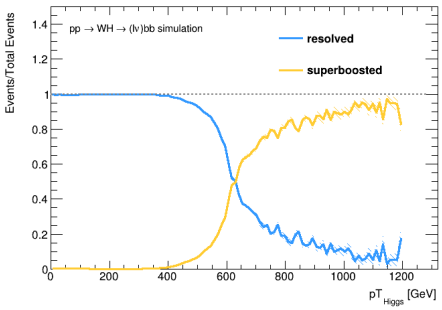

a) Fraction of passed events to total events.

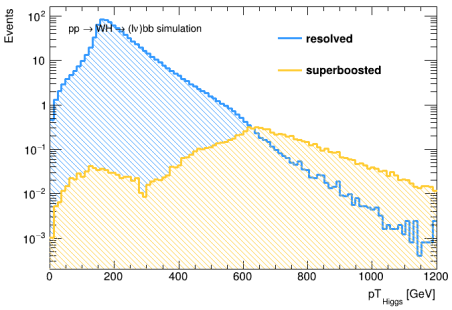

b) Total number of passed events.

Figure 34: Truth Reconstruction characterisations for resolved, superboosted. Plotted as functions of p_T^H.

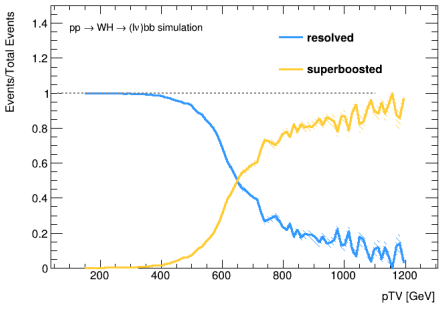

a) Fraction of passed events to total events.

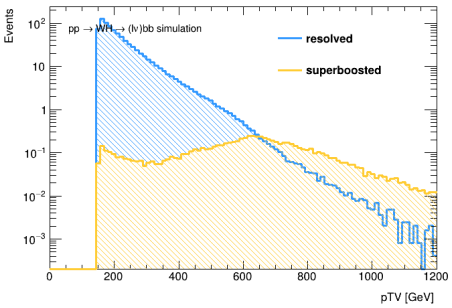

b) Total number of passed events.

Figure 35: Truth Reconstruction characterisations for resolved, superboosted. Plotted as functions of p_T^V. The number of events in a certain energy interval is given in table 3

Only Boosted - Only Superboosted– Overlap Boosted & Superboosted

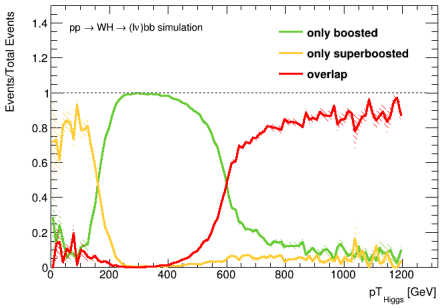

a) Fraction of passed events to total events.

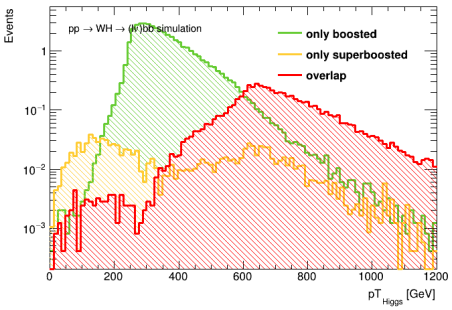

b) Total number of passed events.

Figure 36: Truth Reconstruction characterisations for only boosted, only superboosted, overlap boosted & superboosted. Plotted as functions of p_T^H.

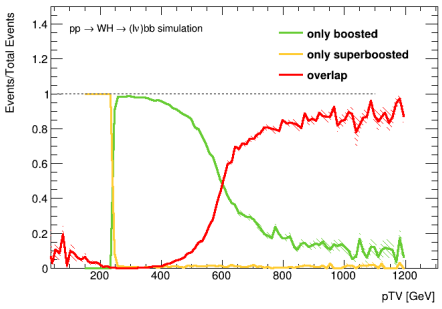

a) Fraction of passed events to total events.

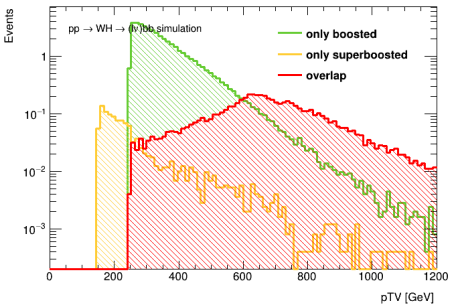

b) Total number of passed events.

Figure 37: Truth Reconstruction characterisations for only boosted, superboosted, overlap boosted & superboosted. Plotted as functions of p_T^V. The number of events in a certain energy interval is given in table 4

Truth Tables

Only Resolved – Superboosted– Only Boosted – Resolved & Boosted

Table 2: Expected number of passed events for different combinations of reconstructions as a function of p_T^V, using truth simulations. The events selected indicate the amount of events that pass the conditions associated to a certain reconstruction out of simulated runs with $7.320 \cdot 10^6$ total events..

(a) Only Resolved

p_T^V [GeV]	Events Selected
[0, 200]	457.366
[201, 400]	301.659
[401, 600]	3.267
[601, 800]	0.174
[801, 1000]	0.0189

(b) Superboosted

p_T^V [GeV]	Events Selected
[0, 200]	0.506
[201, 400]	1.233
[401, 600]	2.530
[601, 800]	3.133
[801, 1000]	1.245

(c) Only Boosted

p_T^V [GeV]	Events Selected
[0, 200]	0.0
[201, 400]	33.924
[401, 600]	10.124
[601, 800]	1.273
[801, 1000]	0.201

(d) Resolved & Boosted

p_T^V [GeV]	Events Selected
[0, 200]	0.0
[201, 400]	109.508
[401, 600]	28.862
[601, 800]	2.305
[801, 1000]	0.247

(e) Sum

p_T^V [GeV]	Events Selected
[0, 200]	457.872
[201, 400]	446.308
[401, 600]	44.784
[601, 800]	6.884
[801, 1000]	1.712

Resolved – Superboosted

Table 3: Expected number of passed events for different combinations of reconstructions as a function of p_T^V, using truth simulations. The events selected indicate the amount of events that pass the conditions associated to a certain reconstruction out of simulated runs with $7.320 \cdot 10^6$ total events.

(a) Resolved

p_T^V [GeV]	Events Selected
[0, 200]	457.383
[201, 400]	411.291
[401, 600]	32.718
[601, 800]	2.695
[801, 1000]	0.299

(b) Superboosted

p_T^V [GeV]	Events Selected
[0, 200]	0.506
[201, 400]	1.233
[401, 600]	2.530
[601, 800]	3.133
[801, 1000]	1.245

(c) Sum

p_T^V [GeV]	Events Selected
[0, 200]	457.890
[201, 400]	412.526
[401, 600]	35.247
[601, 800]	5.828
[801, 1000]	1.544

Only Boosted - Only Superboosted– Overlap Boosted & Superboosted

Table 4: Expected number of passed events for different combinations of reconstructions as a function of p_T^V, using truth simulations. The events selected indicate the amount of events that pass the conditions associated to a certain reconstruction out of simulated runs with $7.320 \cdot 10^6$ total events.

(a) Only Boosted

p_T^V [GeV]	Events Selected
[0, 200]	0.0
[201, 400]	33.924
[401, 600]	10.124
[601, 800]	1.273
[801, 1000]	0.201

(b) Only Superboosted

p_T^V [GeV]	Events Selected
[0, 200]	0.489
[201, 400]	0.601
[401, 600]	0.121
[601, 800]	0.0362
[801, 1000]	0.0105

(c) Overlap Boosted & Superboosted

p_T^V [GeV]	Events Selected
[0, 200]	0.0
[201, 400]	0.500
[401, 600]	1.820
[601, 800]	2.881
[801, 1000]	1.201

(d) Sum

p_T^V [GeV]	Events Selected
[0, 200]	0.506
[201, 400]	35.658
[401, 600]	14.474
[601, 800]	7.287
[801, 1000]	2.647

Reco Plots

Only Resolved – Superboosted– Only Boosted – Resolved & Boosted

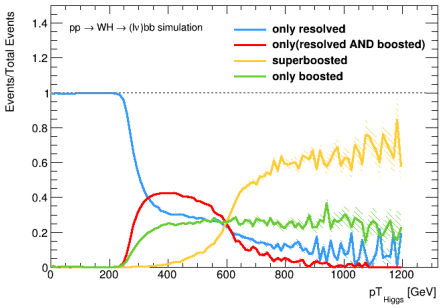

a) Fraction of passed events to total events.

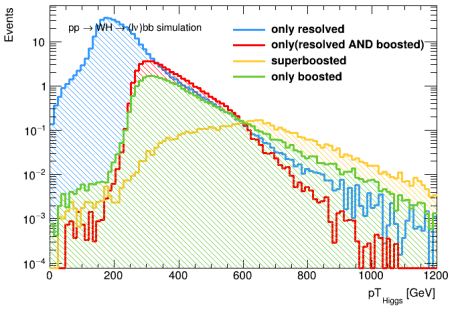

b) Total number of passed events.

Figure 38: Reco Reconstruction characterisations for only resolved, superboosted, only boosted, resolved & boosted. Plotted as functions of p_T^H.

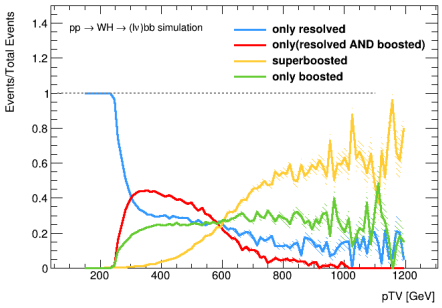

a) Fraction of passed events to total events.

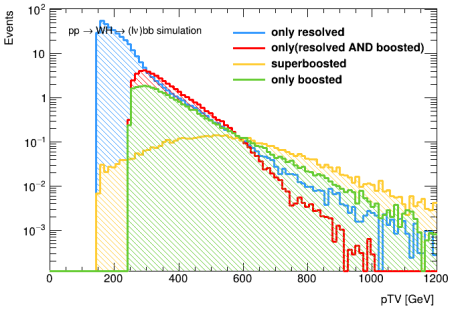

b) Total number of passed events.

Figure 39: Reco Reconstruction characterisations for only resolved, superboosted, only boosted, resolved & boosted. Plotted as functions of p_T^V. The number of events in a certain energy interval is given in table 5

Resolved – Superboosted

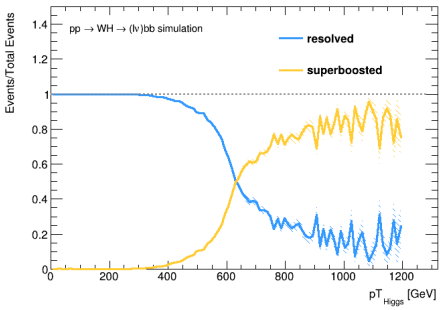

a) Fraction of passed events to total events.

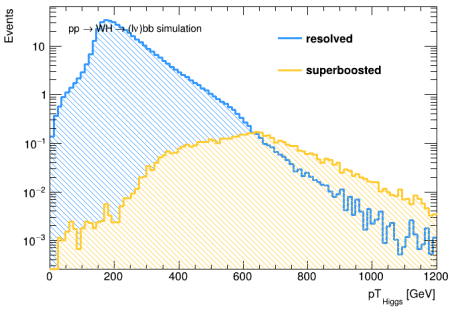

b) Total number of passed events.

Figure 40: Reco Reconstruction characterisations for resolved, superboosted. Plotted as functions of p_T^H.

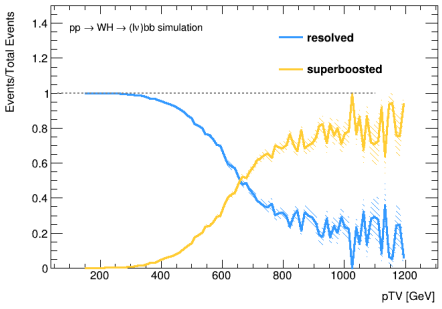

a) Fraction of passed events to total events.

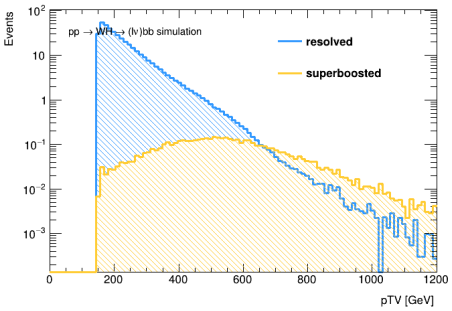

b) Total number of passed events.

Figure 41: Reco Reconstruction characterisations for resolved, superboosted. Plotted as functions of p_T^V. The number of events in a certain energy interval is given in table 6

Only Boosted - Only Superboosted– Overlap Boosted & Superboosted

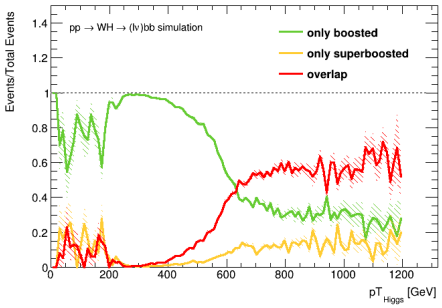

a) Fraction of passed events to total events.

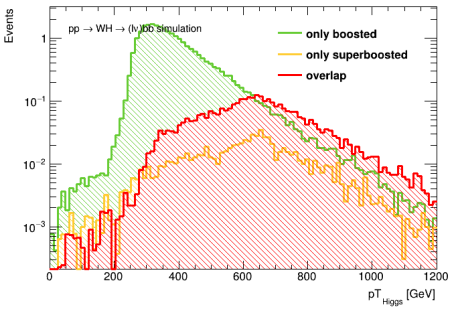

b) Total number of passed events.

Figure 42: Reco Reconstruction characterisations for only boosted, only superboosted, overlap boosted & superboosted. Plotted as functions of p_T^H.

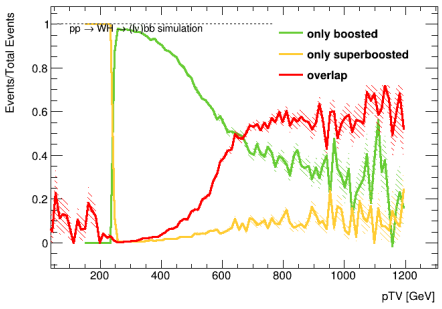

a) Fraction of passed events to total events.

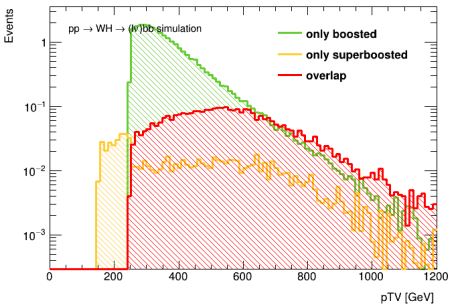

b) Total number of passed events.

Figure 43: Reco Reconstruction characterisations for only boosted, superboosted, overlap boosted & superboosted. Plotted as functions of p_T^V. The number of events in a certain energy interval is given in table 7

Reco Tables

Only Resolved – Superboosted– Only Boosted – Resolved & Boosted

Table 5: Expected number of passed events for different combinations of reconstructions as a function of p_T^V, using reco simulations. The events selected indicate the amount of events that pass the conditions associated to a certain reconstruction out of simulated runs with $7.320 \cdot 10^6$ total events.

(a) Only Resolved

p_T^V [GeV]	Events Selected
[0, 200]	207.114
[201, 400]	172.814
[401, 600]	7.154
[601, 800]	0.665
[801, 1000]	0.0935

(b) Superboosted

p_T^V [GeV]	Events Selected
[0, 200]	0.113
[201, 400]	1.228
[401, 600]	2.318
[601, 800]	1.308
[801, 1000]	0.408

(c) Only Boosted

p_T^V [GeV]	Events Selected
[0, 200]	0
[201, 400]	19.044
[401, 600]	6.346
[601, 800]	0.974
[801, 1000]	0.202

(d) Resolved & Boosted

p_T^V [GeV]	Events Selected
[0, 200]	0
[201, 400]	37.395
[401, 600]	9.509
[601, 800]	0.446
[801, 1000]	0.0241

(e) Sum

p_T^V [GeV]	Events Selected
[0, 200]	207.227
[201, 400]	230.481
[401, 600]	25.328
[601, 800]	3.393
[801, 1000]	0.728

Resolved – Superboosted

Table 6: Expected number of passed events for different combinations of reconstructions as a function of p_T^V, using reco simulations. The events selected indicate the amount of events that pass the conditions associated to a certain reconstruction out of simulated runs with $7.320 \cdot 10^6$ total events.

(a) Resolved

p_T^V [GeV]	Events Selected
[0, 200]	207.120
[201, 400]	210.421
[401, 600]	17.188
[601, 800]	1.287
[801, 1000]	0.151

(b) Superboosted

p_T^V [GeV]	Events Selected
[0, 200]	0.113
[201, 400]	1.228
[401, 600]	2.318
[601, 800]	1.308
[801, 1000]	0.408

(c) Sum

p_T^V [GeV]	Events Selected
[0, 200]	207.233
[201, 400]	211.648
[401, 600]	19.506
[601, 800]	2.595
[801, 1000]	0.560

Only Boosted - Only Superboosted– Overlap Boosted & Superboosted

Table 7: Expected number of passed events for different combinations of reconstructions as a function of p_T^V, using reco simulations. The events selected indicate the amount of events that pass the conditions associated to a certain reconstruction out of simulated runs with $7.320 \cdot 10^6$ total events.

(a) Only Boosted

p_T^V [GeV]	Events Selected
[0, 200]	0
[201, 400]	19.044
[401, 600]	6.346
[601, 800]	0.974
[801, 1000]	0.202

(b) Only Superboosted

p_T^V [GeV]	Events Selected
[0, 200]	0.108
[201, 400]	0.316
[401, 600]	0.235
[601, 800]	0.168
[801, 1000]	0.0624

(c) Overlap Boosted & Superboosted

p_T^V [GeV]	Events Selected
[0, 200]	0
[201, 400]	0.700
[401, 600]	1.559
[601, 800]	0.964
[801, 1000]	0.312

(d) Sum

p_T^V [GeV]	Events Selected
[0, 200]	0.113
[201, 400]	20.972
[401, 600]	10.224
[601, 800]	3.246
[801, 1000]	0.923

Backgrounds

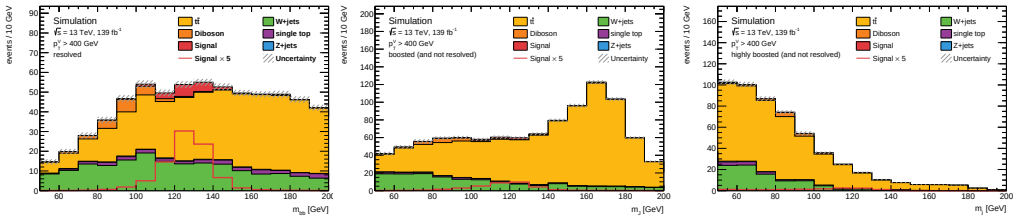

a) Resolved
Z = 0.984

b) Boosted
Z = 0.332

c) Superboosted
Z = 0.158

Figure 44: Background rejection for resolved, boosted and superboosted at $p_T^V > 400$ GeV. The significance Z is given as $s/\sqrt{s+b}$ where s is the signal and b is the background and is calculated using all events in the window between 100 GeV and 140 GeV.

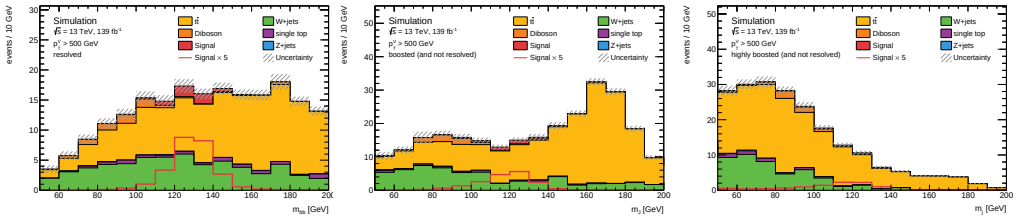

a) Resolved
Z = 0.536

b) Boosted
Z = 0.355

c) Superboosted
Z = 0.193

Figure 45: Background rejection for resolved, boosted and superboosted at $p_T^V > 500$ GeV. The significance Z is given as $s/\sqrt{s+b}$ where s is the signal and b is the background and is calculated using all events in the window between 100 GeV and 140 GeV.

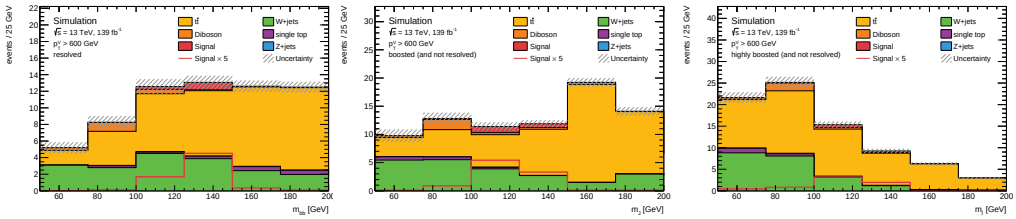

a) Resolved
Z = 0.245

b) Boosted
Z = 0.362

c) Superboosted
Z = 0.207

Figure 46: Background rejection for resolved, boosted and superboosted at $p_T^V > 600$ GeV. The significance Z is given as $s/\sqrt{s+b}$ where s is the signal and b is the background and is calculated using all events in the window between 100 GeV and 140 GeV.

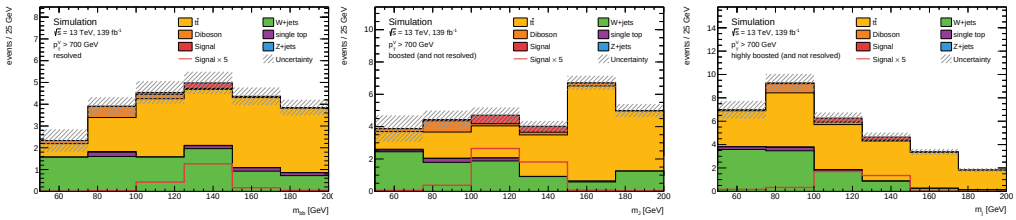

a) Resolved
Z = 0.109

b) Boosted
Z = 0.302

c) Superboosted
Z = 0.185

Figure 47: Background rejection for resolved, boosted and superboosted at $p_T^V > 700$ GeV. The significance Z is given as $s/\sqrt{s+b}$ where s is the signal and b is the background and is calculated using all events in the window between 100 GeV and 140 GeV.

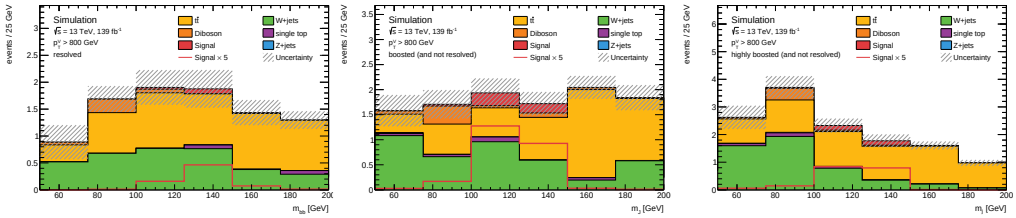

a) Resolved
Z = 0.0640

b) Boosted
Z = 0.230

c) Superboosted
Z = 0.161

Figure 48: Background rejection for resolved, boosted and superboosted at $p_T^V > 800$ GeV. The sensitivity Z is given as $s/\sqrt{s+b}$ where s is the signal and b is the background and is calculated using all events in the window between 100 GeV and 140 GeV.

Appendix C. Main backgrounds for $W \to \ell\nu$ $H \to b\bar{b}$

$t\bar{t}$ production

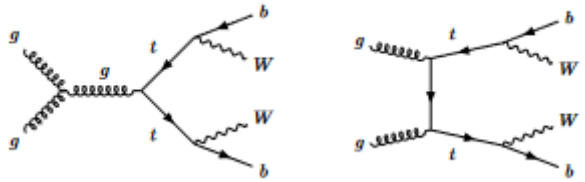

Figure 49: Example first-order Feynman diagrams for $t\bar{t}$ production with subsequent $t \to Wb$ decay [23].

W+jets production

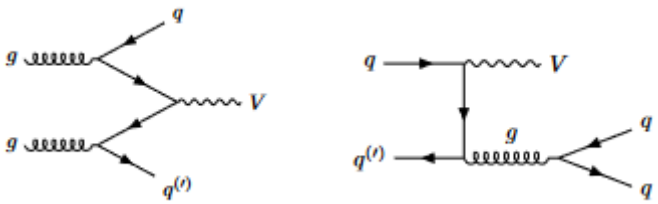

Figure 50: Example first-order Feynman diagrams for V+jets production. In this thesis, V is taken to be the W boson [23].